Project No. 10-941

Consistent Multigroup Theory Enabling Accurate Coarse-Group Simulation of GenIV Reactors

Reactor Concepts RD&D

Dr. Farzad Rahnema
Georgia Institute of Technology

In collaboration with:
Idaho National Laboratory
Virginia Polytechnic Institute and State University

Rob Versluis, Federal POC
Abderrafi Ougouag, Technical POC

NEUP Nuclear Energy University Programs
U.S. Department of Energy

NEUP PROJECT FINAL REPORT

Project Title: Consistent Multigroup Theory Enabling Accurate Coarse-Group Simulation of Gen-IV Reactors

Covering Period: July 18, 2010 through September 30, 2013

Date of Report: November 30, 2013

Recipient: Georgia Institute of Technology
770 State Street NW
Atlanta, GA 30332-0425

Project Number: 10-941

Principal Investigator: Farzad Rahnema,
Phone: 404-894-3731
Email: farzad@gatech.edu

Collaborators: Dingkang Zhang, Georgia Institute of Technology, dingkang.zhang@gatech.edu
Alireza Haghighat, Virginia Tech, haghigha@vt.edu
Abderrafi Ougouag, Idaho National Laboratory, Abderrafi.Ougouag@inl.gov

SUMMARY

The standard multi-group method used in whole-core reactor analysis relies on energy condensed (coarse-group) cross sections generated from single lattice cell calculations, typically with specular reflective boundary conditions. Because these boundary conditions are an approximation and not representative of the core environment for that lattice, an error, known as core environment effect, is introduced in the core solution (both eigenvalue and flux). As current and next generation reactors trend toward increasing assembly and core heterogeneity, this error becomes more significant. Additionally, the angular dependence of the coarse-group total cross section for whole-core calculation is commonly ignored. The consistent energy condensation method corrects for both effects by generating updated coarse-group cross sections on-the-fly within whole-core reactor calculations without resorting to additional cell calculations and explicitly accounting for the angular dependence of the coarse-group total cross section. The core environment effect is fully corrected by making use of the recently published Generalized Energy Condensation Theory to unfold the fine-group core flux and recondense the cross sections at the whole-core level. By iteratively performing this recondensation, an improved core solution is found in which the core environment effect has been fully taken into account. Furthermore, the energy-angle coupling effect in the coarse-group calculation is accounted for by modifying the treatment of the total cross section to include orthogonal expansions in both energy and angle. As a result, the fine-group flux can be consistently reproduced during the coarse-group calculation. This recondensation method is both easy to implement and computationally very efficient because it requires pre-computation and storage of only the energy integrals and fine-group cross sections.

Moreover, the consistent generalized energy condensation method was extended to subgroup decomposition method. The subgroup decomposition method enables the cross section condensation process by preserving spectral accuracy in condensed-group transport calculations in a simpler and more direct manner, without the need for the expansion in energy. The new "group decomposition" method directly couples a consistent coarse-group criticality calculation with a set of fixed-source "decomposition sweeps" to obtain the fine-group spectrum without the need to solve for higher energy moments of the flux.

Also, the subgroup decomposition method which was developed in pure transport theory has been extended to pure diffusion and hybrid quasi transport/transport theories. The culmination of the works related to subgroup decomposition method confirms that the method is in fact an acceleration technique for solving fine-group eigenvalue transport (diffusion) problems.

I. PROJECT OVERVIEW

Project Objective:

The objective of the project is the development of a consistent multi-group theory that accurately accounts for the energy-angle coupling associated with collapsed group cross sections. This will allow for coarse-group transport and diffusion theory calculations that exhibit continuous energy accuracy and implicitly treat cross-section resonances. This is of particular importance when considering the highly heterogeneous and optically thin reactor designs within the NGNP framework. In such reactors, ignoring the influence of anisotropy in the angular flux on the collapsed cross section, especially at the interface between core and reflector near which control rods are located, results in inaccurate estimates of the rod worth, a serious safety concern. The scope of this project will include the development and verification of a new multi-group theory enabling high fidelity transport and diffusion calculations in coarse groups, as well as a methodology for the implementation of this method in existing codes. This will allow for

higher accuracy solution of reactor problems while using fewer groups and reduce the computational expense. The proposed research represents a fundamental advancement in the understanding and improvement of multi-group theory for reactor analysis.

Background:

The multi-group formulation represents a discretization of the energy variable in the transport and diffusion equations that is necessary to allow for the solution of reactor problems. The first step in the implementation of the multi-group method is the integration of the transport equation from continuous energy into a set of equations over discrete energy groups *g*.

This formulation requires the definition of multi-group parameters (cross-sections) within each group. The multi-group cross sections are generated by performing an average of the cross sections over a set of coarse energy intervals. This naturally leads to generating the total group cross section as an average over each group, weighted by the angular flux, leading to the total group cross section becoming angularly dependent. Most available transport codes do not allow for an angular dependent multi-group cross section, and the standard remedy is to remove the angular dependence of the total cross section by assuming the flux is separable in energy and angle. This assumption clearly breaks down in problems in which the flux is highly anisotropic, as is in optically thin problems or local regions. This is the case in regions possessing strong heterogeneity (in and around absorbers, near boundaries, or any region where sharp flux gradients are encountered) or within fast energy groups in general. The trend in reactor design (Gen-IV, advanced, and operating reactors) is towards increased heterogeneity for improved fuel economy. As a result, the effect of energy-angle coupling becomes more pronounced even in current reactor designs.

Products:

The products developed as a result of this project are listed below:

1. Consistent generalized energy condensation method
    - Derived in general geometry and continuous energy
    - Implemented in 1D slab geometry and multi-group theory
2. Subgroup decomposition method in neutron transport theory
    - Derived in general geometry and continuous energy
    - Implemented in 1D, 2D and 3D geometries and multi-group theory
3. Subgroup decomposition method in neutron diffusion theory
    - Derived in general geometry and continuous energy
    - Implemented in 1D slab geometry and multi-group theory
4. Hybrid subgroup decomposition method for solving fine-group eigenvalue transport problems
    - Derived in general geometry and continuous energy
    - Implemented in 1D slab geometry and multi-group theory

II. PUBLICATIONS

This section lists the publications that resulted from this project.

Journal papers:

1. F. Rahnema, S. Douglass, and B. Forget, "A Generalized Energy Condensation Theory," *Nucl. Sci. Eng*, **160,** No. 1, 41-58 (2008).
2. S. Douglass and F. Rahnema, "Cross Section Recondensation Method via Generalized Energy Condensation Theory," Technical Note, *Ann. Nucl. Energy*, **38**, 2105–2110 (2011)
3. S. Douglass and F. Rahnema, "Consistent Generalized Energy Condensation Theory," *Ann. Nucl. Energy*, **40**, 200–214 (2012).
4. S. Douglass and F. Rahnema, "Subgroup Decomposition Method," *Ann. Nucl. Energy*, **48**, 84-101 (2012).
5. S. Yasseri and F. Rahnema "Subgroup Decomposition Method in Diffusion Theory," *Ann. Nucl. Energy*, *Ann. Nucl. Energy*, **60**, 235–241 (2013).
6. S. Yasseri and F. Rahnema, "Hybrid subgroup decomposition method for solving fine-group eigenvalue transport problems", *Ann. Nucl. Energy*, Submitted (October 2013).

Conference papers:

1. S. Douglass, F. Rahnema, and R. Szilard, "2-Dimensional Recycling Reactor Whole Core Benchmark Problem," *Advances in Nuclear Fuel Management IV (ANFM 2009)* Hilton Head Island, South Carolina, USA, April 12-15, 2009, on CD-ROM, American Nuclear Society, LaGrange Park, IL (2009).
2. S. Douglass, F. Rahnema, and B. Forget, "2-Dimenational PWR and BWR Whole Core Benchmark Problems," *International Conference on Mathematic, Computational Methods & Reactor Physics (M&C 2009)*, Saratoga Spring, New York, May 3-7, 2009, on CD-ROM, American Nuclear Society, LaGrange Park, IL (2009).
3. S. Douglass and F. Rahnema, "Analysis of Cross-Section Condensation in PWR Simulations" *PHYSOR 2010 – Advances in Reactor Physics to Power the Nuclear Renaissance*, Pittsburgh, Pennsylvania, USA, May 9-14, 2010, on CD-ROM, American Nuclear Society, LaGrange Park, IL (2010)
4. S. Douglass and F. Rahnema, "A Whole Core BWR Benchmark Problem," *The Joint International Conference of the 7th Supercomputing in Nuclear Application and the 3rd Monte Carlo (SNA + MC2010)*, Tokyo, Japan, October 17 – 21, on CD-ROM (2010).
5. S. Douglass and F. Rahnema, "Spectral Correction for Nuclear Data in Fast Reactor Analysis via the Subgroup Decomposition Method," *ENC 2012 – The European Forum to discuss Nuclear Technology Issues, Opportunities & Challenges*, 9 -12 December 2012, Manchester, United Kingdom (2012).
6. S. Yasseri and F. Rahnema, "Application of Subgroup Decomposition in Diffusion Theory for Gas Cooled Thermal Reactor Problems," *International Conference on Mathematics and Computational Methods Applied to Nuclear Science & Engineering (M&C 2013)*, Sun Valley, Idaho, USA, May 5-9, 2013, on CD-ROM, American Nuclear Society, LaGrange Park, IL (2013).
7. F. Rahnema and S. Yasseri, "On the consistent Spatial Homogenization Method in Neutron Transport Theory," *International Conference on Transport Theory (ICTT 23)*, Santa Fe, NM, USA, September 15-20, 2013.
8. S. Yasseri and F. Rahnema, "Simultaneous Energy Condensation and Spatial Homogenization of Cross Sections in Transport Theory," *International Conference on Transport Theory (ICTT 23)*, Santa Fe, NM, USA, September 15-20, 2013.

III. PROJECT TASKS

Task 1.1 Derive a new multi-group transport equation in general geometry incorporating energy-angle coupling and all equations necessary to generate the multi-group constants (cross sections).

Within the derivation of the Generalized Energy Condensation Theory [1], the total cross section within each group is separated into two terms: the scalar flux-averaged total group cross section and a "variation" cross section, which is the deviation of the energy dependence of the cross section from the group-average, as in Eq. (1.1.1).

$$\sigma(\vec{r},u) = \sigma_g(\vec{r}) + \delta(\vec{r},u) \tag{1.1.1}$$

where

$$\sigma_g(\vec{r}) = \frac{\int_g du\sigma(\vec{r},u)\varphi(\vec{r},u)}{\int_g du\varphi(\vec{r},u)} \tag{1.1.2}$$

The essential premise of the GEC theory is to expand the energy dependence of the flux in a complete set of orthogonal functions $\xi_n(u)$ with weighting function *w(u)* within each coarse group, as in Eq. (1.1.3).

$$\begin{aligned} \Psi(\vec{r},\hat{\Omega},u\in g) &= \sum_n \alpha_n \Psi_{ng}(\vec{r},\hat{\Omega})\xi_n(u\in g) \\ \Psi_{ng}(\vec{r},\hat{\Omega}) &= \int_g du\Psi(\vec{r},\hat{\Omega},u)w(u)\xi_n(u) \end{aligned} \tag{1.1.3}$$

Because the flux is used as the weighting function in the condensation process, this expansion allows the coarse-group cross sections to include higher-order moments which are not present in the standard condensation. Each coarse group is scaled to the lethargy interval of the group, and when this expansion is incorporated into the transport equation, the generalized condensed transport equation is the result, presented in Eq. (1.1.4).

$$\begin{aligned} &\hat{\Omega}\cdot\nabla\Psi_{ng}(\vec{r},\hat{\Omega}) + \sigma_g(\vec{r})\Psi_{ng}(\vec{r},\hat{\Omega}) + \delta_{ng}(\vec{r},\hat{\Omega})\Psi_{0g}(\vec{r},\hat{\Omega}) \\ &= \sum_{g'=1}^{G}\sum_{l=0}^{\infty}\sum_{m=-l}^{l}\frac{Y_{lm}^*(\hat{\Omega})}{4\pi}\int_g duw(u)\xi_n(u)\int_{g'} du'\sigma_{sl}(\vec{r},u'\to u)\Psi_{lm}(\vec{r},u') \\ &+ \sum_{g'=1}^{G}\frac{\chi_{ng}(\vec{r})}{4\pi k}\int_{g'} du'\nu\sigma_f(\vec{r},u')\phi(\vec{r},u') \end{aligned} \tag{1.1.4}$$

In Eq. (1.1.4), the scattering kernel has been expanded in spherical harmonics for consistency with the derivation of the GEC theory; however, this is not a requirement of the method. Additional information concerning the derivation of Eq. (1.1.4), including detailed definitions of each of the terms may be found in [1]. Of note in this equation is that, as a result of the separation of the collision cross section into two terms, the coupling of the energy and angular dependence within each coarse group has been entirely shifted from the traditional collision rate into the variation term $\delta_{ng}(\vec{r},\hat{\Omega})\Psi_{0g}(\vec{r},\hat{\Omega})$, which is defined in Eq. (1.1.5).

$$\delta_{ng}(\vec{r},\hat{\Omega})\Psi_{0g}(\vec{r},\hat{\Omega}) = \int_g du(\sigma(\vec{r},u) - \sigma_g(\vec{r}))\Psi(\vec{r},\hat{\Omega},u)w(u)\xi_n(u) \tag{1.1.5}$$

In the original formulation of the GEC theory, this variation term was addressed by assuming that the energy and angular dependence of the flux were separable, just as in standard multi-group theory. Therefore, within the context of the GEC theory, this is the term that must be addressed by the consistent multigroup method. The new method begins by approximating the angular flux in Eq. (1.1.5) by a series expansion of the angular variable in spherical harmonics [2], as in Eq. (1.1.6). It is noted that other expansion bases may be used to treat this angular dependence [3]. The selection of basis may be best determined by optimizing for the specific solution method used to solve the resulting transport equations in the system (e.g., core).

$$\Psi(\vec{r},\hat{\Omega},u) = \sum_{l=0}^{\infty}\sum_{m=-l}^{l}\Psi_{lm}(\vec{r},u)Y_{lm}(\hat{\Omega}) \tag{1.1.6}$$

The angular expansion coefficients of the flux are defined in Eq. (1.1.7).

$$\phi_{lm}(\vec{r},u) = \int_{4\pi} d\hat{\Omega}\Psi(\vec{r},\hat{\Omega},u)Y^*_{lm}(\hat{\Omega}) \quad l = 0,...,\infty \quad m = -l,...,l \tag{1.1.7}$$

Where $Y_{lm}(\hat{\Omega})$ and $Y^*_{lm}(\hat{\Omega})$ are the spherical harmonic functions and their complex conjugates, respectively [2]. When Eqs. (1.1.6) and (1.1.7) are inserted into the RHS of Eq. (1.1.5), an expansion (in energy and angle) of the variation term results, as in Eq. (1.1.8).

$$\delta_{ng}(\vec{r},\hat{\Omega})\Psi_{0g}(\vec{r},\hat{\Omega}) = \sum_{l=0}^{\infty}\sum_{m=-l}^{l}\int_g du(\sigma(\vec{r},u) - \sigma_g(\vec{r}))w(u)\xi_n(u)Y_{lm}(\hat{\Omega})\int_{4\pi} d\hat{\Omega}'\Psi(\vec{r},\hat{\Omega}',u)Y^*_{lm}(\hat{\Omega}') \tag{1.1.8}$$

This is then simplified to Eq. (1.1.9)

$$\delta_{ng}(\vec{r},\hat{\Omega})\Psi_{0g}(\vec{r},\hat{\Omega}) = \sum_{l=0}^{\infty}\sum_{m=-l}^{l}\delta^{lm}_{ng}(\vec{r})Y_{lm}(\hat{\Omega})\phi_g(\vec{r}) \tag{1.1.9}$$

by defining the expansion coefficients of the variation cross section as in Eq. (1.1.10).

$$\delta_{ng}^{lm}(\vec{r}) = \frac{\int_g du(\sigma(\vec{r},u) - \sigma_g(\vec{r}))w(u)\xi_n(u)\int_{4\pi} d\hat{\Omega}'\Psi(\vec{r},\hat{\Omega}',u)Y_{lm}^*(\hat{\Omega}')}{\int_g du\int_{4\pi} d\hat{\Omega}'\Psi(\vec{r},\hat{\Omega}',u)} \tag{1.1.10}$$

Replacing the variation term in Eq. (1.1.4) with Eq. (1.1.9), and moving it to the RHS generates the consistent multi-group equations, presented in Eq. (1.1.11).

$$\begin{aligned}\hat{\Omega}\cdot\nabla\Psi_{ng}(\vec{r},\hat{\Omega}) + \sigma_g(\vec{r})\Psi_{ng}(\vec{r},\hat{\Omega}) = &\sum_{g'=1}^{G}\sum_{l=0}^{\infty}\sum_{m=-l}^{l}\frac{Y_{lm}^*(\hat{\Omega})}{4\pi}\sigma_{slm}^{n,g'\to g}(\vec{r})\phi_{lm,g'}(\vec{r}) \\ &+ \sum_{g'=1}^{G}\frac{\chi_{ng}(\vec{r})}{4\pi k}\nu\sigma_{fg'}(\vec{r})\phi_{g'}(\vec{r}) - \sum_{l=0}^{\infty}\sum_{m=-l}^{l}\delta_{ng}^{lm}(\vec{r})Y_{lm}(\hat{\Omega})\phi_g(\vec{r})\end{aligned} \tag{1.1.11}$$

where the multi-group coefficients for the scattering and fission cross sections, and angular flux moments have been defined as in Eqs. (1.1.12) – (1.1.14).

$$\sigma_{slm}^{n,g'\to g}(\vec{r}) = \frac{\int_g duw(u)\xi_n(u)\int_{g'} du'\sigma_{sl}(\vec{r},u'\to u)\phi_{lm}(\vec{r},u')}{\int_{g'} du'\phi_{lm}(\vec{r},u')} \tag{1.1.12}$$

$$\nu\sigma_{fg'}(\vec{r}) = \frac{\int_{g'} du'\nu\sigma_f(\vec{r},u')\phi(\vec{r},u')}{\int_{g'} du'\phi(\vec{r},u')} \tag{1.1.13}$$

$$\chi_{ng}(\vec{r}) = \int_g du\chi(\vec{r},u)w(u)\xi_n(u) \tag{1.1.14}$$

$$\phi_{lm,g'}(\vec{r}) = \int_{g'} du'\phi_{lm}(\vec{r},u') \tag{1.1.15}$$

Equations (1.1.11) - (1.1.15) represent a multi-group formulation of the transport equation, the solution of which is fully consistent with the fine-group energy and angular dependence. In addition, because the consistent method is based on the GEC theory, the fine-group flux may be extracted from the coarse-group solution. As a result, the consistent multi-group theory results in fine-group accuracy within a coarse-group calculation.

As in the standard multi-group method for whole-core problems, the fine-group (or continuous energy) flux used as the weighting function is computed for a lattice cell (fuel assembly with specular reflective boundaries), and this flux is used to condense the cross sections in Eqs. (1.1.2), (1.1.10), (1.1.12), and (1.1.13). Once these condensed cross sections and variation coefficients are computed, the coarse-group core flux moments may be obtained from Eq. (1.1.11) using any solution method (discrete ordinates, characteristics, etc.). It is noted that if one strictly uses discrete ordinates with the same number of ordinates for both core and assembly level calculations, one could treat the variation term as defined at specific directional values in the same manner as the angular flux. Using an expansion of the angular dependence in the variation term (e.g., spherical harmonics), however, provides a more general consistent formulation which is applicable to a wider array of solution methods. As a result, the spherical harmonics expansion was used to test the method. Also of note is the fact that the variation term in Eq. (1.1.11) does not depend on the higher order moments of the flux (in angle or energy), and is dependent only on the scalar group flux. This allows the consistent multi-group method to provide a significantly improved solution over the standard multi-group method without impacting the solution time.

Task 1.2 Generate 1D benchmark problems representative of optically thin reactors

One of the most challenging aspects of optically thin reactors is that the increased anisotropy and longer mean free paths of these systems generate significant spectral errors in the condensed cross sections. As a result, a larger number of coarse groups are generally required to generate accurate core solutions. While this requires more than 20 coarse groups in some systems (e.g., high temperature gas cooled reactors), as few as 6 groups are often used to obtain more rapid solutions; however, the 2-group structure generally used in LWR problems is unable to accurately represent the optically thin spectrum with the standard method. One of the advantages of the consistent method is that, because the condensed solution exactly reproduces the fine-group reaction rates, the accuracy of the solution becomes much less dependent on the coarse-group structure.

In order to demonstrate the effectiveness of the consistent method to accurately treat an optically thin problem with a coarse-group structure that is not optimal for the problem, a 1D benchmark problem was selected which is characteristic of gas cooled prismatic block reactor systems. The detailed parameters and the method of development of the benchmark problem, which is based on the HTTR core, are presented in [4]. The core consists of eight blocks of 4 types: Fuel 1, Fuel 2, Fuel 3, Control Rod Block (CRB), and Reflectors, laid out as in Fig. 1.2.1, with specular reflective boundary condition on the right, vacuum boundary conditions on the left.

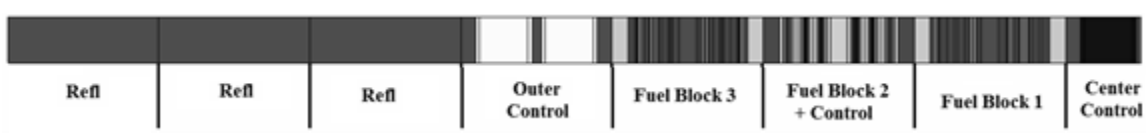

Fig. 1.2.1. 1D HTTR Benchmark Problem Layout

Task 1.3 Formulate the theory in 1D geometry and implement in a 1D transport code

While the consistent multi-group theory is generalized so that any orthogonal set of functions may be used to expand the energy dependence, in practice, Legendre Polynomials are a logical choice. Because the weighting function $w(u)$ is equal to unity and the non-0th order moments integrate to zero, the RHS of Eq. (1.1.11) depends only on the 0th energy expansion order (n=0) flux [1]. As a result, the 0th energy

expansion order equation accounts for the full integral quantities (eigenvalue, coarse-group flux, etc.), and the higher order equations are only used to extract the fine-group flux, as in the GEC theory. Thus, the primary value in the consistent multi-group formulation of the variation term is the correction when n=0.

While the consistent multi-group method is sufficiently general to be applicable in any dimensions and with any order of scattering or angular approximation, for the sake of clarity, the method is implemented in 1D with isotropic scattering. The 1D form of the consistent multi-group equations is presented in Eq. (1.3.1), with isotropic scattering.

$$\mu \frac{d}{dx}\Psi_{ng}(x,\mu)+\sigma_g(x)\Psi_{ng}(x,\mu)=\frac{1}{2}\sum_{g'=1}^{G}\sigma_s^{n,g'\to g}(x)\phi_{g'}(x) + \sum_{g'=1}^{G}\frac{\chi_{ng}(x)}{2k}\nu\sigma_{fg'}(x)\phi_{g'}(x)-\sum_{l=0}^{L}\delta_{ng}^{l}(x)P_l(\mu)\phi_g(x) \tag{1.3.1}$$

While either a continuous energy or fine-group structure may serve as the weighting function for the consistent multi-group method, for the purposes of report a fine-group structure is used, and the equations are solved in a discrete ordinates framework. The expansion of the variation term is truncated after $L+1$ terms of the angular expansion. The number of terms does not significantly affect the solution time in 1D, and the number of terms kept is generally determined by the available order of angular expansion of the fine-group flux. For example, if the fine-group flux is obtained with a discrete ordinates calculation, a maximum of N terms (L=N-1) may be approximated with the quadrature methods inherent in discrete ordinates calculations.

Task 1.4 Generate collapsed cross sections from continuous energy

Fundamental to any reactor analysis is the accurate calculation of cross section data/libraries. In this task, MoCSgen [5] has been used to generate cross sections for a prismatic HTR problem. The MoCSgen code, developed recently at Georgia Institute of Technology, is an advanced and robust stochastic cross section generation tool capable of producing accurate cross section libraries including scattering kernels with arbitrary Legendre expansion order for deterministic/Monte Carlo and diffusion theory whole core calculations. Since MoCSgen is based on continuous energy Monte Carlo, there is no inherent constraint with respect to geometry, material or energy spectrum.

The HTR problem is obtained from the INEEL/EXT-04-02331 report [6] and ANL-GenIV-075 report [7]. The core configuration is shown in Fig. 1.4.1. In this problem, a fuel block consists of 204 fuel pins, 108 coolant channels, and 6 BP pins. The BP pin cell is defined as a 0.93 cm-radius cylindrical region containing the BP pin with some adjacent graphite as shown in Figure 1.4.2. There are 102 fuel blocks in the whole HTR core. The detailed description of geometry and material compositions can be found in the references INEEL/EXT-04-02331 and ANL-GenIV-075.

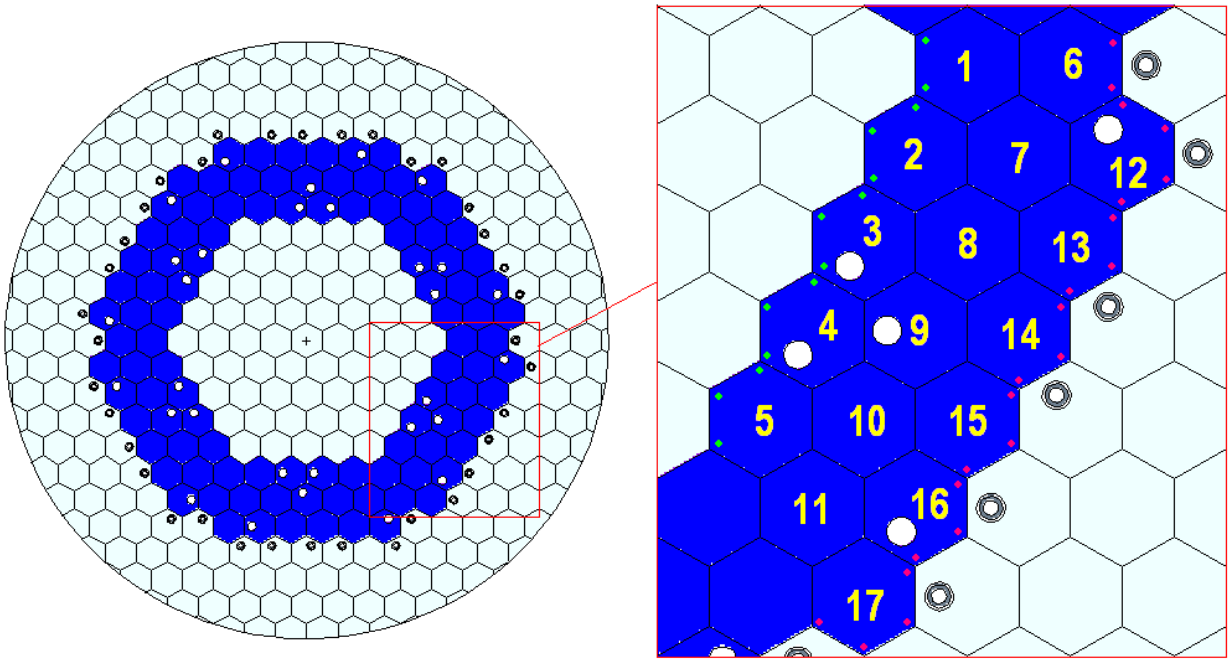

Fig. 1.4.1 HTR whole core layout and fuel block indexing

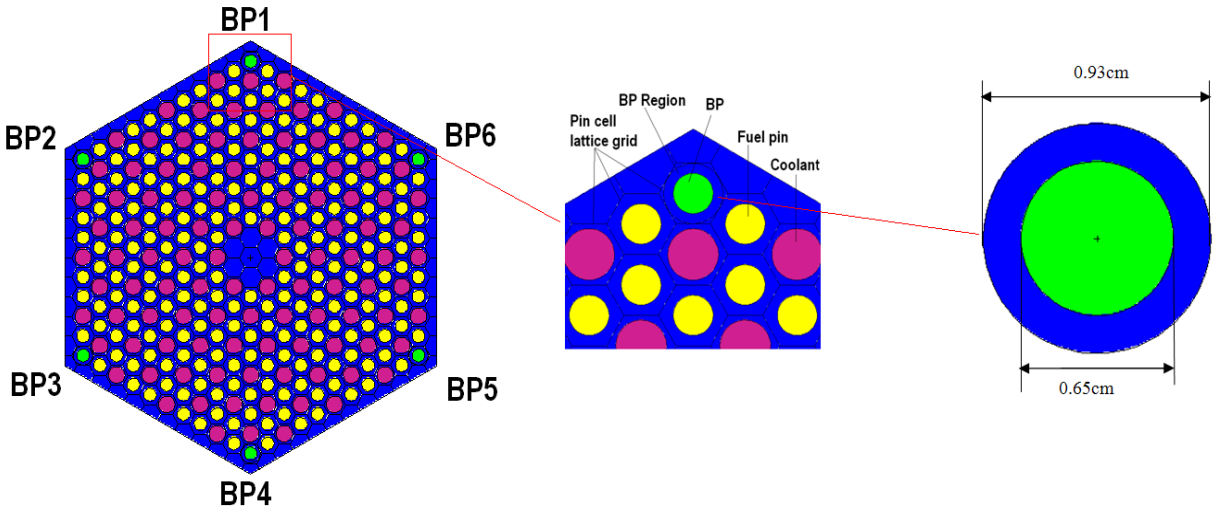

Figure 1.4.2 Fuel block and burnable pin configuration

MoCSgen was used to generate 7-group cross sections for the HTR problem described above.

Task 1.5 Use selected codes to generate standard multi-group solutions

The multi-group solutions for 1D benchmark problems are described in details in section 2.1 as well as [8].

Task 2.1 Implement the theory into the selected codes in 1D and solve 1D benchmarks

The primary objective of the consistent multi-group method, within the framework of GEC theory, is to allow for the generation of high-resolution energy information of the angular flux within an arbitrarily coarse multi-group energy structure. There are two orders of expansion contained within the consistent generalized equations. The first (N) is the number of higher order energy moments that are preserved to allow unfolding the detailed energy dependence during the coarse-group calculation. The second (L) is the order of the coupling correction included in the source term of the coarse-group calculation. As a result, L dictates the accuracy of the coarse-group calculation, and N dictates the degree of detailed flux spectrum that may be unfolded from it.

The first phase of verification is to examine the accuracy of the coarse-group calculation without unfolding (N=0). This is presented in the following sections for several 1D transport problems by comparison of the accuracy of the coarse-group transport solution (eigenvalue, flux) using the consistent multi-group method with that obtained using the standard method.

2.1.1 1D Test Problems (N=0)

Cross section condensation is generally performed at the lattice cell level, because the whole-core flux weighting function is not known *a priori*. However, the specular reflective boundary conditions which are typically used for the lattice calculation are not a good representation of the angular flux in the core, and thus the use of these boundary conditions introduces a core-environment error [4] and simultaneously masks the energy-angle coupling effect by assuming a more isotropic flux than is actually present. In order to avoid these assumptions, the bundle problems used to verify the consistent method use boundary conditions taken from the interface flux in a core calculation. This isolates the consistent condensation method from the effect of core environment error and increases the anisotropy of the flux distribution, creating a more challenging problem and highlighting the influence of the energy-angle coupling effect.

In order to verify the method, two bundle types are selected from a recently published 1D BWR benchmark problem [4]. Each bundle is composed of 10 material regions (8 fuel-pin regions + moderator region on both sides). The fuel regions are each 1.6256 cm in width, and the outside moderator regions are 1.1176 cm in width, accounting for 15.24 cm total bundle width (typical of BWR bundles). The two bundle types are laid out in Fig. 2.1.1. Bundle A is composed of low-enriched pins (“L”), high-enriched pins (“H”), and moderator (“M”). Bundle B is composed of both low-enriched fuel pins and gadded fuel pins (“G”).

M	L	L	H	H	H	H	L	L	M

(a) Bundle A

M	L	L	G	G	G	G	L	L	M

(b) Bundle B

Fig. 2.1.1. Single Bundle Layout for Bundles A and B

In order to obtain boundary conditions for the bundles which are representative of a core environment, Core 2 of the 1D BWR benchmark problem [4] is used. This core possesses steep flux gradients and highly anisotropic flux across the assembly interfaces due to alternating fuel bundles and partially gadded fuel bundles. Also of note is that this benchmark problem, which was constructed by layering pin-cell homogenized cross sections, does not represent a 1D core directly, but rather was designed to more accurately represent local transport effects (e.g., flux at a gadded pin-cell interface). The core is composed of seven bundles, with vacuum boundaries on both sides, shown with the 2-group flux in Fig. 2.1.2. The 47-group reference eigenvalue, computed with an S_{16} approximation was 1.05595. The 47-group cross section library was generated with HELIOS v1.10 [9] using a GE9 pin-cell model, homogenized over the pin cells in the same manner as [4].

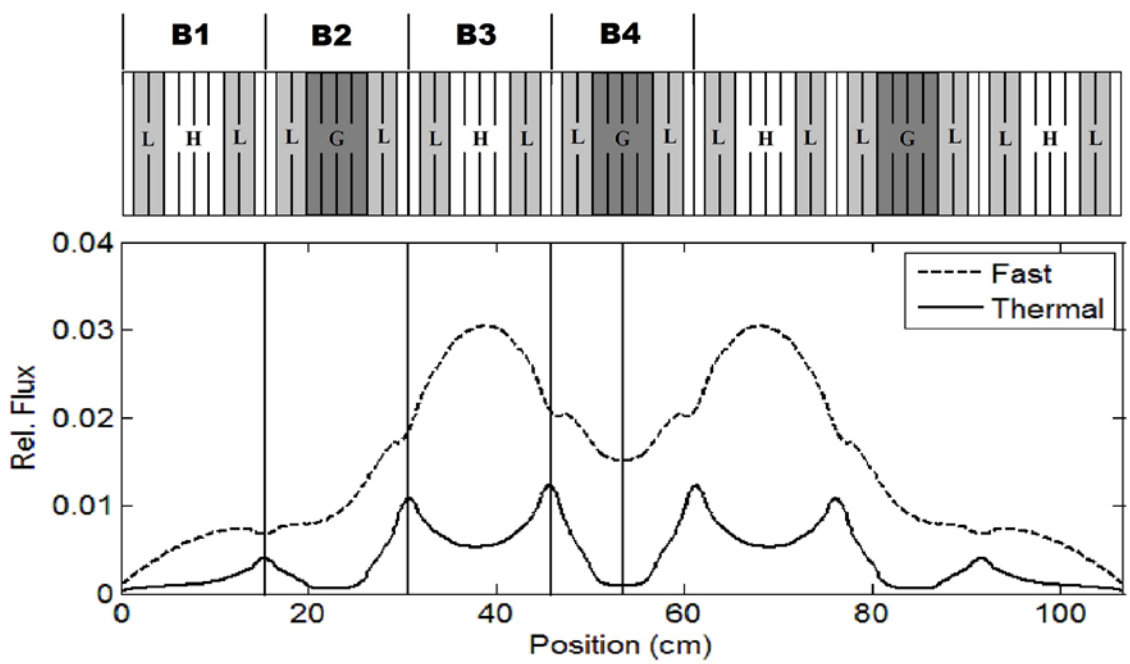

Fig. 2.1.2. 1D Core Layout and 2g Flux. Vertical lines on the flux graph represent bundle interfaces. Center line is the symmetry line of the core.

The core calculation was used only to provide 47-group core-level boundary conditions for the bundles. Because the boundary conditions vary by bundle position in the core, there are four unique bundles labeled in Fig. 2.1.2: (B1) Periphery, (B2) Outer Gadded, (B3) Inner Fuel, and (B4) Center Gadded.

For each bundle, the following method is used to verify the consistent multi-group method.

1. A 47-group transport calculation is performed with an S_{16} approximation and albedo boundary conditions from the core calculation. This flux is the reference solution for the bundle.
2. The 47-group reference angular flux is used to generate 2-group cross sections using both the standard method (assuming separable energy and angle) and the consistent condensation theory (with energy-angle coupling correction).
3. These cross sections are then used to solve the bundle problem in a 2-group, S_{16} calculation with boundary conditions obtained by integrating the 47-group boundary conditions into the 2-group structure.
4. The 2-group solution is compared to the 47-group reference solution (eigenvalue, scalar and angular flux).

Because the accuracy of the new method is determined by how well the 2-group solution matches the 47-group solution, an initial verification of the method is obtained by comparing the eigenvalue of the 2-group calculation (k_2) with the 47-group reference eigenvalue (k_{47}). The eigenvalue results of the calculations are presented in Table 2.1.1. Because the 47-group solution was computed with an S_{16} calculation, the variation term is limited to 15th order, and is therefore truncated at L=15. The standard multi-group method corresponds to the 0th-order energy-angle correction (L=0).

Table 2.1.1. Eigenvalue results for Bundles 1-4 for increasing angular expansion order.

	Bundle 1		Bundle 2		Bundle 3		Bundle 4	
$k_{47}ref$[1]	1.05597		1.05599		1.05599		1.05599	
	k_2	δk^* *(pcm)*	k_2	δk^* *(pcm)*	k_2	δk^* *(pcm)*	k_2	δk^* *(pcm)*
Standard Method	1.10384	4787	1.17632	12034	1.07804	2205	1.08593	2994
L = 1	1.05565	-33	1.05135	-464	1.05526	-73	1.05163	-436
L = 2	1.05653	56	1.05564	-35	1.05618	19	1.05572	-27
L = 3	1.05608	11	1.05560	-39	1.05608	9	1.05565	-34
L = 4	1.05594	-3	1.05609	10	1.05595	-4	1.05607	7
L = 5	1.05599	1	1.05593	-5	1.05600	1	1.05594	-5
L = 6	1.05594	-3	1.05604	6	1.05597	-2	1.05604	5
L = 7	1.05597	-1	1.05598	-1	1.05599	0	1.05598	-1
L = 8	1.05596	-1	1.05600	2	1.05598	-1	1.05600	1
L = 9	1.05597	-1	1.05598	0	1.05599	0	1.05599	0
L = 10	1.05596	-1	1.05599	0	1.05598	-1	1.05599	0
L = 11	1.05597	0	1.05598	0	1.05599	0	1.05599	0
L = 12	1.05597	0	1.05598	0	1.05599	0	1.05599	0
L = 13	1.05597	0	1.05598	0	1.05599	0	1.05599	0
L = 14	1.05597	0	1.05598	0	1.05599	0	1.05599	0
L = 15	1.05597	0	1.05599	0	1.05599	0	1.05599	0

$\delta k^* = 10^5 (k_2 - k_{47}ref)$

[1] The 47 group reference eigenvalue is determined from the single bundle calculation with boundary conditions obtained from the core calculation, and is expected to match the core eigenvalue within numerical convergence criteria.

Table 2.1.1 clearly demonstrates both the magnitude of error introduced by assuming the energy and angular dependence are separable and the effectiveness of the consistent method to correct this error. Particularly in the gadded bundles (2 and 4), the anisotropy introduced by the strong absorber resulted in significant errors. As seen in the table, a 3rd order correction is sufficient to account for most of the effect of the energy-angle coupling, and a 7th order correction is sufficient to fully account for it.

In addition to the eigenvalues, verification of the consistent multi-group method requires an examination of the accuracy of the flux solution, both with the standard and consistent multi-group methods. For each bundle, the 2-group flux (angular and scalar) is compared with the 2-group flux obtained by integrating the 47-group reference into the 2-group structure.

2.1.2 Bundle 1 Flux Comparison

Because the consistent method is designed to better account for flux anisotropy in the coarse-group calculation, both the scalar and angular flux accuracy must be examined. Fig. 2.1.3 contains the 2-group reference scalar flux as a function of position in the bundle and the 2-group reference angular flux, averaged over the bundle, for each discrete direction. The angular flux is normalized such that the magnitude of each arrow in the figure represents the fraction of the angular flux in that direction (i.e. the sum of the magnitude for all directions is 100 for each group).

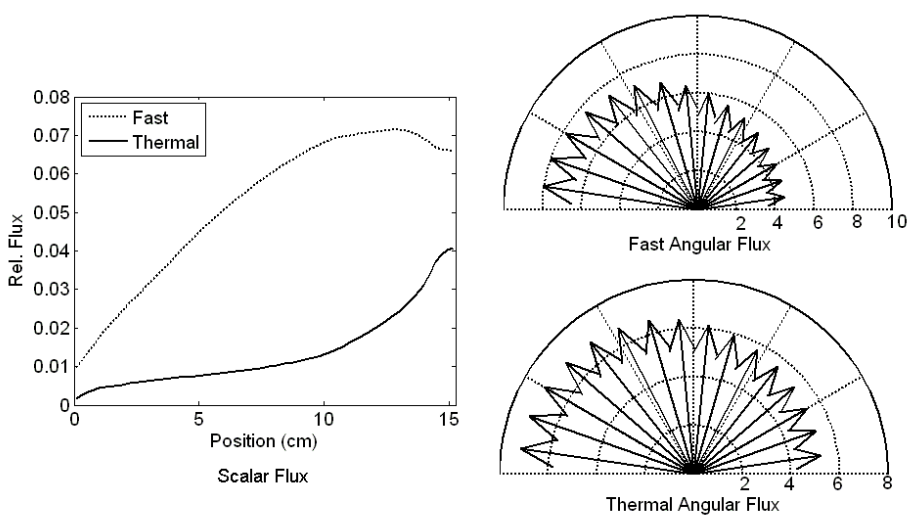

Fig. 2.1.3. Bundle 1 - Reference Scalar Flux and Spatially Averaged Angular Flux (2g)

The anisotropy of the flux in this bundle is clearly seen in Fig. 2.1.3, particularly in the fast group, wherein neutrons are streaming towards the vacuum boundary on the left hand side. In order to examine the accuracy of the coarse group calculation using both the standard method and the consistent multi-group method, the 2g flux error is presented in Fig. 2.1.4. The scalar flux error is presented for the standard method, a first-order coupling correction (L=1), and the full coupling correction (L=15). For the angular flux, only the standard method and the L=1 case are presented because the error of the fully corrected (L=15) solution is too small to be visible on the figure.

As seen in Fig. 2.1.4, the standard multi-group method results in significant errors in both the scalar and angular flux distributions. In the scalar flux, it is clearly seen that this error increases towards the vacuum boundary where the flux is more anisotropic. In addition, the angular distribution shows that the

error in the fast group is, as expected, highly dependent on the direction. Fig. 2.1.4 also demonstrates that even the 1st order corrected solution generates significant improvement over the standard multi-group method in both the scalar and angular fluxes and that the 15th order correction was able to reproduce the reference solution exactly. Note that in order to allow for easy viewing of the angular flux errors, it was necessary to use a different scale for the fast and the thermal flux errors.

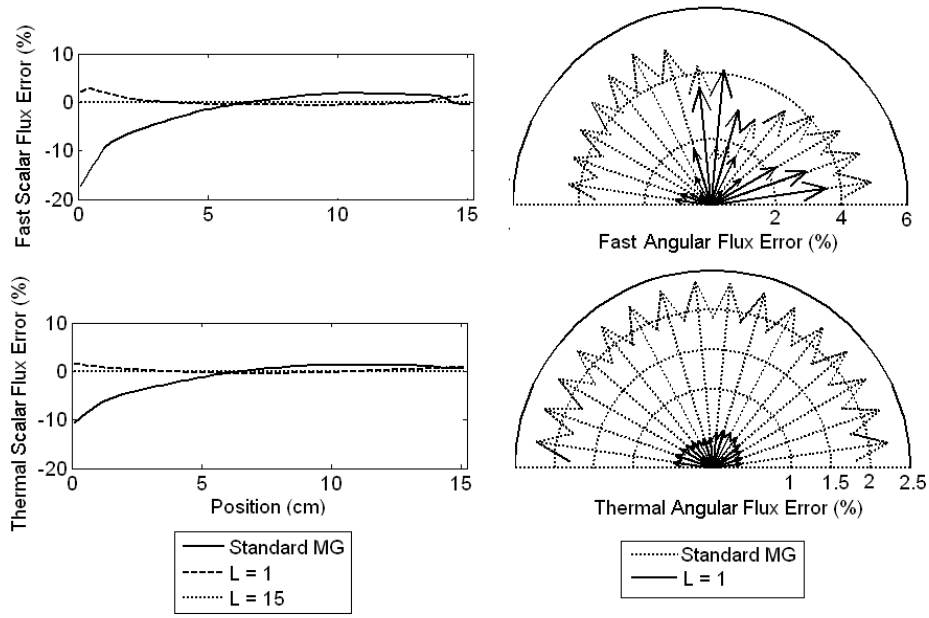

Fig. 2.1.4. 2g Scalar and Average Angular Flux %-Error for Bundle 1.

In order to gain a more thorough understanding of the error present in the scalar flux distribution, the 2-group scalar flux from the condensed calculation $\tilde{\varphi}_g(x)$ was compared with the reference 2-group scalar flux $\varphi_g(x)$ using the AVG, RMS, and MRE errors, defined in Eqs. (2.1.1-2.1.4). Table 2.1.2 presents these errors for increasing order of coupling correction in Bundle 1.

$$AVG_g = \frac{\int dx \left| e_g(x) \right|}{\int dx} \tag{2.1.1}$$

$$RMS_g = \sqrt{\frac{\int dx e_g^2(x)}{\int dx}} \tag{2.1.2}$$

$$MRE_g = \frac{\int dx \left| e_g(x) \right| \tilde{\phi}_g(x)}{\int dx \phi_g(x)} \tag{2.1.3}$$

where

$$e_g(x) = 100 \frac{\tilde{\phi}_g(x) - \phi_g(x)}{\phi_g(x)} \tag{2.1.4}$$

As is seen in Table 2.1.2, the flux results are quite poor for the standard multi-group method, resulting in an average error greater than 2%. When using even a 1st order coupling correction, this is reduced to less than 1%, and by the 3rd order the consistent multi-group method has reproduced the reference solution with high accuracy. It is also evident from the results in Table 2.1.2 that the energy-angle coupling of the total cross section can be fully accounted for with accuracy sufficient for the vast majority of purposes by a 4th or 5th order correction. This is true of Bundle 1, presented here, as well as for the other bundles, which are shown in the next sections.

Table 2.1.2. Scalar Flux Error Analysis – Bundle 1

	AVG (%)		RMS (%)		MRE (%)	
L	Fast	Thermal	Fast	Thermal	Fast	Thermal
0*	2.92	2.15	4.58	3.15	1.83	1.34
1	0.67	0.40	0.90	0.50	0.56	0.42
2	0.13	0.07	0.21	0.10	0.13	0.12
3	0.06	0.03	0.10	0.04	0.05	0.03
4	0.04	0.01	0.07	0.02	0.04	0.02
5	0.02	0.00	0.04	0.01	0.02	0.00
6	0.02	0.00	0.04	0.01	0.02	0.01
7	0.01	0.00	0.03	0.00	0.01	0.00
8	0.02	0.00	0.03	0.00	0.02	0.00
9	0.01	0.00	0.02	0.00	0.01	0.00
10	0.01	0.00	0.02	0.00	0.01	0.00
11	0.01	0.00	0.01	0.00	0.01	0.00
12	0.01	0.00	0.01	0.00	0.01	0.00
13	0.00	0.00	0.01	0.00	0.00	0.00
14	0.00	0.00	0.01	0.00	0.00	0.00
15	0.00	0.00	0.00	0.00	0.00	0.00

* L = 0 is the Standard Multigroup Method

2.1.3 Bundle 2 Flux Comparison

Fig. 2.1.5 contains the 2-group reference scalar flux as a function of position in the bundle and the 2-group reference angular flux, averaged over the bundle, for each discrete direction.

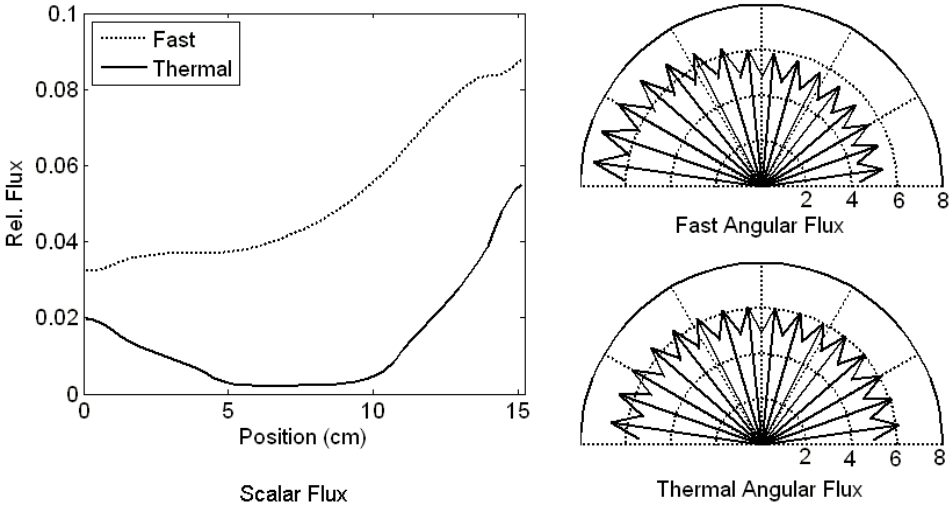

Fig. 2.1.5. Bundle 2 - Reference Scalar Flux and Spatially Averaged Angular Flux (2g)

In this bundle, there is a significantly high anisotropy in the angular flux because of the presence of the gadolinium. (This anisotropy is not evident in Fig. 2.1.5 because the strong gradients on both sides of the bundle result in a highly anisotropic flux in opposite directions.) This results in much larger flux errors than in Bundle 1. The scalar flux error is presented for the standard method, a first-order coupling correction (L = 1), and the full coupling correction (L=15) in Fig. 2.1.6.

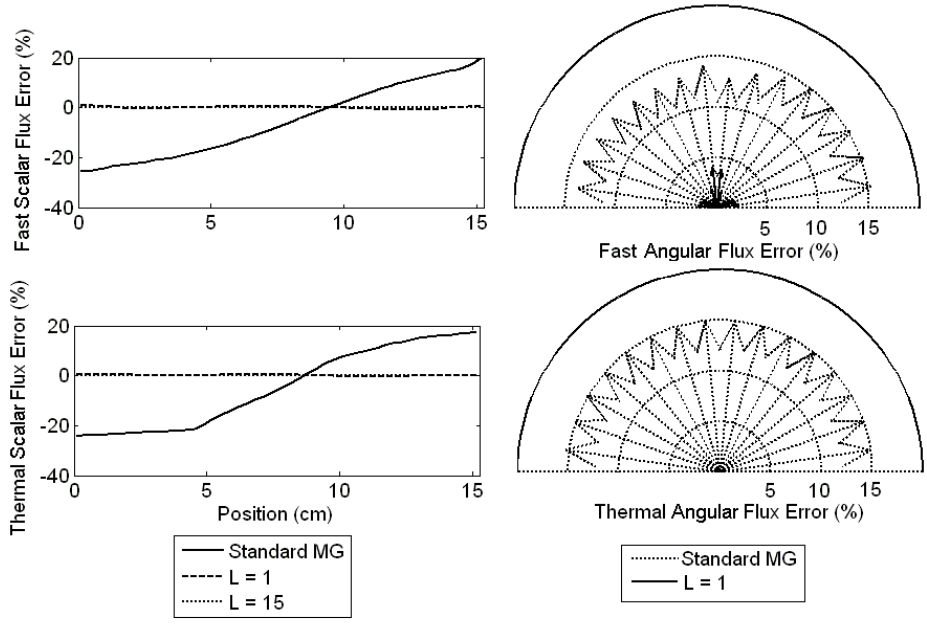

Fig. 2.1.6. 2g Scalar and Average Angular Flux %-Error for Bundle 2.

As seen in Fig. 2.1.6, the standard multi-group method results in much larger errors in the flux than in Bundle 1. This is due to the increased effect of local anisotropies generated by the strong flux gradient across the bundle. It is also evident that in this bundle, the 1st order coupling correction results in significant improvement. It is noted that the 1st order error in the thermal angular flux is too small to be

visible on the graph. Table 2.1.3 presents the AVG, RMS, and MRE errors for increasing order of coupling correction in Bundle 2.

Table 2.1.3. Scalar Flux Error Analysis – Bundle 2

	AVG (%)		RMS (%)		MRE (%)	
L	Fast	Thermal	Fast	Thermal	Fast	Thermal
0*	13.42	14.71	15.25	16.28	12.11	16.98
1	0.42	0.27	0.50	0.31	0.44	0.18
2	0.17	0.09	0.21	0.10	0.18	0.09
3	0.07	0.03	0.09	0.03	0.08	0.03
4	0.05	0.02	0.09	0.02	0.06	0.02
5	0.03	0.00	0.04	0.01	0.03	0.00
6	0.03	0.01	0.05	0.01	0.03	0.01
7	0.02	0.00	0.03	0.00	0.02	0.00
8	0.02	0.00	0.04	0.01	0.02	0.00
9	0.01	0.00	0.02	0.00	0.01	0.00
10	0.01	0.00	0.02	0.00	0.01	0.00
11	0.01	0.00	0.01	0.00	0.01	0.00
12	0.01	0.00	0.02	0.00	0.01	0.00
13	0.00	0.00	0.01	0.00	0.00	0.00
14	0.00	0.00	0.01	0.00	0.00	0.00
15	0.00	0.00	0.00	0.00	0.00	0.00

* L = 0 is the Standard Multigroup Method

It is clear from Table 2.1.3 that Bundle 2 is much more greatly affected by neglecting the energy angle coupling using the standard method; however, a 1st order coupling correction is sufficient to reproduce the fine-group results very well.

2.1.4 Bundle 3 Flux Comparison

Fig. 2.1.7 contains the 2-group reference scalar flux as a function of position in the bundle and the 2-group reference angular flux, averaged over the bundle, for each discrete direction.

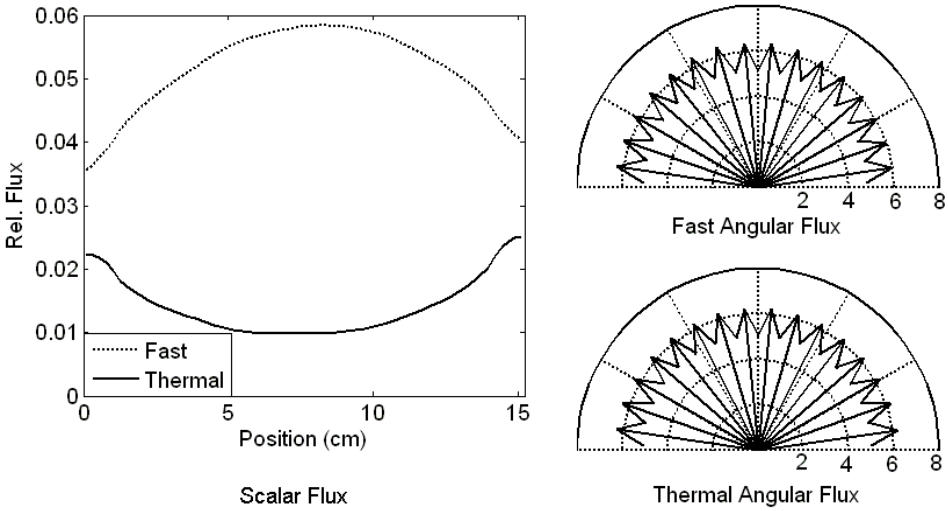

Fig. 2.1.7. Bundle 3 - Reference Scalar Flux and Spatially Averaged Angular Flux (2g)

Because the position of Bundle 3 in the core results in a roughly symmetric flux distribution, and because the bundle does not possess any gadded pins, Bundle 3 is the least anisotropic. This is clearly seen in the angular flux graphs in Fig. 2.1.7. The scalar and angular flux errors are presented in Fig. 2.1.8.

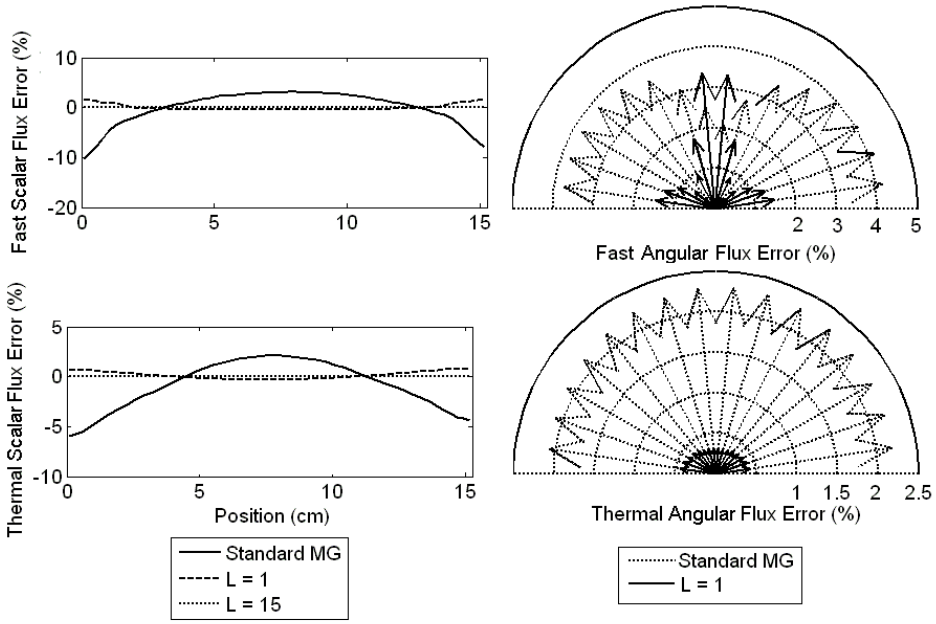

Fig. 2.1.8. 2g Scalar and Average Angular Flux %-Error for Bundle 3.

As seen in Fig. 2.1.8, while the flux error in this bundle is less significant than in bundles 1 and 2, the error is still significant in both the scalar and angular flux distributions using the standard method. As in bundles 1 and 2, the 1st order coupling correction provides a significant improvement over the standard method. Table 2.1.4 presents the AVG, RMS, and MRE errors for Bundle 3, demonstrating similar behavior as previous bundles.

Table 2.1.4. Scalar Flux Error Analysis – Bundle 3

	AVG (%)		RMS (%)		MRE (%)	
L	Fast	Thermal	Fast	Thermal	Fast	Thermal
0*	2.65	2.07	3.36	2.52	2.49	2.34
1	0.49	0.32	0.61	0.39	0.46	0.38
2	0.14	0.06	0.21	0.09	0.12	0.08
3	0.06	0.02	0.09	0.03	0.05	0.03
4	0.04	0.01	0.08	0.02	0.04	0.01
5	0.02	0.00	0.04	0.00	0.02	0.00
6	0.03	0.00	0.05	0.01	0.02	0.01
7	0.02	0.00	0.03	0.00	0.02	0.00
8	0.02	0.00	0.04	0.00	0.02	0.00
9	0.01	0.00	0.02	0.00	0.01	0.00
10	0.01	0.00	0.02	0.00	0.01	0.00
11	0.01	0.00	0.01	0.00	0.01	0.00
12	0.01	0.00	0.02	0.00	0.01	0.00
13	0.00	0.00	0.01	0.00	0.00	0.00
14	0.00	0.00	0.01	0.00	0.00	0.00
15	0.00	0.00	0.00	0.00	0.00	0.00

* L = 0 is the Standard Multigroup Method

2.1.5 Bundle 4 Flux Comparison

Fig. 2.1.9 contains the 2-group reference scalar flux as a function of position in the bundle and the 2-group reference angular flux, averaged over the bundle, for each discrete direction. Whereas the previous bundles have included the full bundle, due to the symmetry of Bundle 4, only half of the bundle was modeled. This allows the local anisotropies present in the bundle to be apparent, as seen in Fig. 2.1.9.

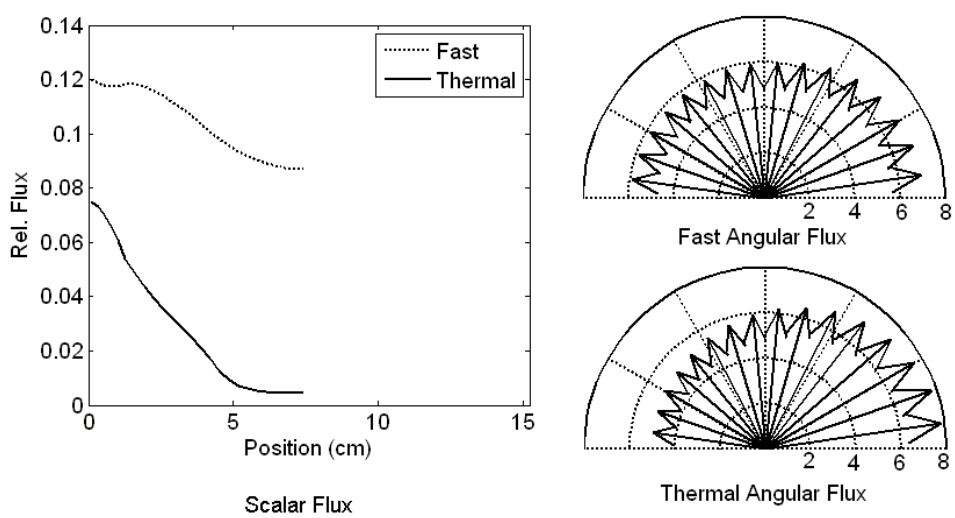

Fig. 2.1.9. Bundle 4 - Reference Scalar Flux and Spatially Averaged Angular Flux (2g)

As seen in Fig. 2.1.9, the angular flux (particularly thermal), is highly directed due to the presence of strong absorbers (gadded pins). In Bundle 2, this effect was averaged out over the whole bundle, but

because only the left half of the bundle is used here, the local anisotropy is more apparent. This indicates that even in the case of specular boundary conditions, local anisotropies may still introduce energy-angle coupling effects that must be considered. The flux errors for Bundle 4 are presented in Fig. 2.1.10.

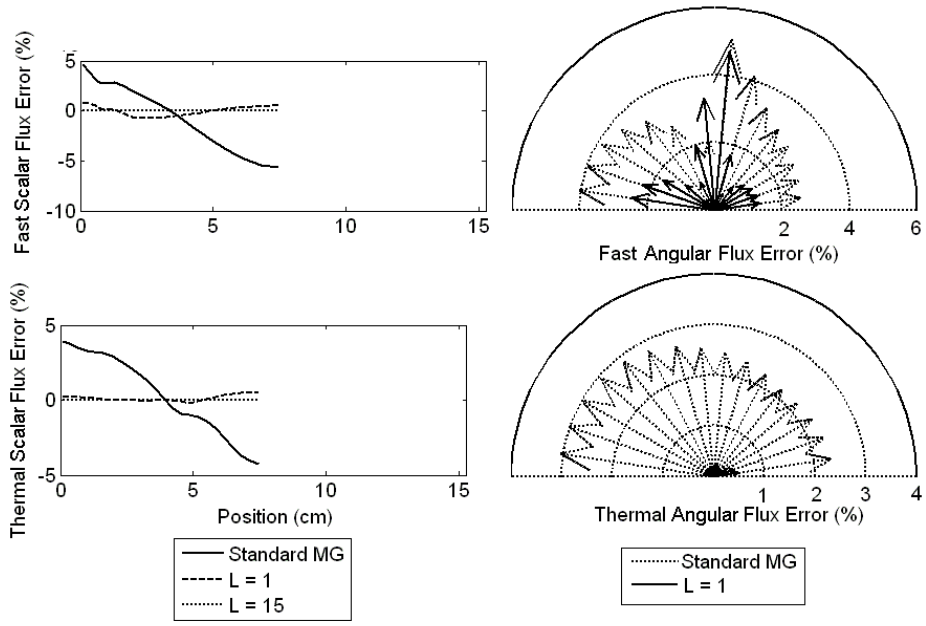

Fig. 2.1.10. 2g Scalar and Average Angular Flux %-Error for Bundle 4.

As in previous bundles, the 1st order coupling correction greatly improved the solution, and the 15th order coupling correction reproduced the reference calculation exactly. Table 2.1.5 presents the AVG, RMS, and MRE errors for increasing order of coupling correction in Bundle 4.

Table 2.1.5. Scalar Flux Error Analysis – Bundle 4

	AVG (%)		RMS (%)		MRE (%)	
L	Fast	Thermal	Fast	Thermal	Fast	Thermal
0*	1.47	1.17	2.40	1.87	2.79	2.77
1	0.21	0.08	0.33	0.16	0.42	0.12
2	0.09	0.03	0.14	0.05	0.18	0.05
3	0.04	0.01	0.06	0.02	0.08	0.03
4	0.03	0.01	0.06	0.01	0.06	0.02
5	0.01	0.00	0.03	0.00	0.03	0.00
6	0.01	0.00	0.04	0.01	0.03	0.01
7	0.01	0.00	0.02	0.00	0.02	0.00
8	0.01	0.00	0.03	0.00	0.02	0.00
9	0.01	0.00	0.02	0.00	0.01	0.00
10	0.01	0.00	0.02	0.00	0.01	0.00
11	0.00	0.00	0.01	0.00	0.01	0.00
12	0.00	0.00	0.01	0.00	0.01	0.00
13	0.00	0.00	0.01	0.00	0.00	0.00
14	0.00	0.00	0.01	0.00	0.00	0.00
15	0.00	0.00	0.00	0.00	0.00	0.00

* L = 0 is the Standard Multigroup Method

Task 2.2 Extend the numerical formulation into 2D

The numerical formulation in 3D explains a more general case and it covers the formulation in 2D. Please refer to section 3.2 for details.

2.3 Generate 2D benchmark problems

In this section we outline our efforts to model a 2D hexagonal fuel assembly from the Simplified 2D HTTR benchmark problem, Zhang et al [10], using the PENTRAN [11] 3-D Cartesian transport theory code system. To benchmark the PENTRAN model, we prepared a reference multi-group MCNP model.

2.3.1 Description of Fuel Assembly

This fuel assembly contains 33 fuel pins of 3.8% enrichment, 4.1 cm diameter, and 100 cm axial length. The assembly also contains 3 burnable poison rods of 1.5 cm diameter. The fuel pitch is 5.15 cm, and flat-to-flat distance of the assembly is 36 cm.

2.3.2 PENTRAN Model

Using the PENMSHXP [12], we have prepared a PENTRAN model as shown in Figure2.3.1.

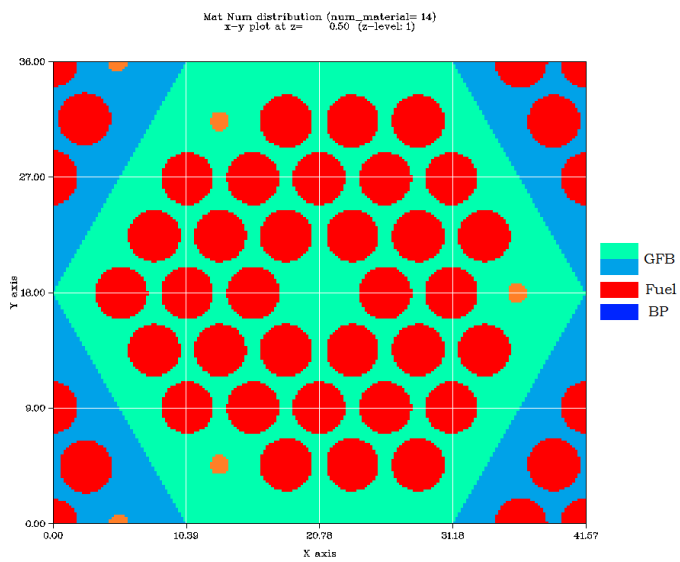

Figure 2.3.1: PENTRAN model for a HTTR fuel assembly.

In the figure above, GFB refers to graphite in the fuel block and BP refers to burnable poison. Note that because of PENTRAN's Cartesian geometry, this model includes segments of the four neighbor assemblies. Of course, this is not a true representation of the fuel assembly, but the purpose of this study is to examine the effectiveness of PENTRAN in modeling a hexagonal lattice using a Cartesian geometry.

In is important to note that the PENTRAN spatial discretization is comprised of coarse and fine meshing. Each coarse mesh is made of a uniform set of fine meshes, while different coarse meshes can have different size of fine meshes.

The model shown in Figure is comprised of 16 coarse meshes, and each coarse mesh contains 50 by 50 fine meshes. A 6-group cross-section library was obtained from Zhang, et al. [10]. Table provides the upper energies of the 6-group structure.

Table 2.3.1: Upper energy of the 6-group library.

Group	Upper Energy (eV)
1	2.00E+07
2	1.83E+05
3	9.61E+02
4	2.38
5	0.65
6	0.105

2.3.3 MCNP Model

Initially the PENTRAN model was compared to the fuel assembly MCNP calculations from Zhang, et al [10]. This model did not include the corner regions that are not technically included in the fuel assembly, but are required for comparison with the PENTRAN model. We therefore developed a new MCNP model that included the corner regions. The MCNP model is shown in Figure .

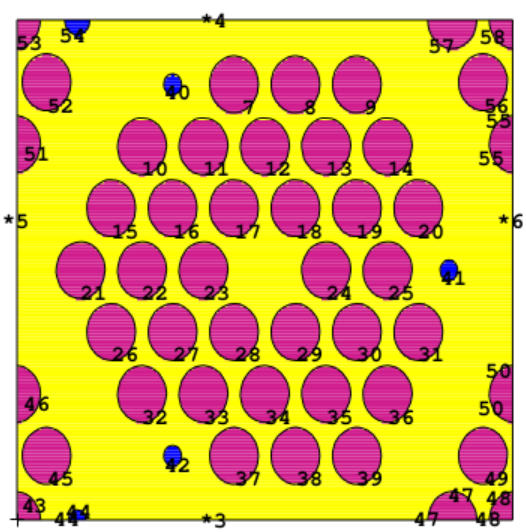

Figure 2.3.2: MCNP fuel assembly model.

MCNP was run with the 6-group cross-section library as used for the PENTRAN calculation.

2.3.4 PENTRAN Calculation Results in Comparison with Reference MCNP Predictions

For the base model, numerical parameters include: i) DTW differencing scheme; ii) system rebalance; iii) S12 angular quadrature set; and, iv) a convergence criterion of 1.0 x10^{-5} (both k and flux). For parallel processing, we use the angular decomposition algorithm on 8 processors. A meshing of 50x50 fine meshes per coarse mesh was used.
Table compares eigenvalues calculated by PENTRAN and MCNP.

Table 2.3.2: Comparison of calculated eigenvalues.

Method	***k*-eigenvalue**	**pcm***
MCNP Monte Carlo	1.15108 (±2 pcm)	0
PENTRAN	1.150414	58

*percent mili reactivity

The PENTRAN eigenvalue is in good agreement with the MCNP prediction. The 6-group neutron flux distributions are presented in Figure , below.

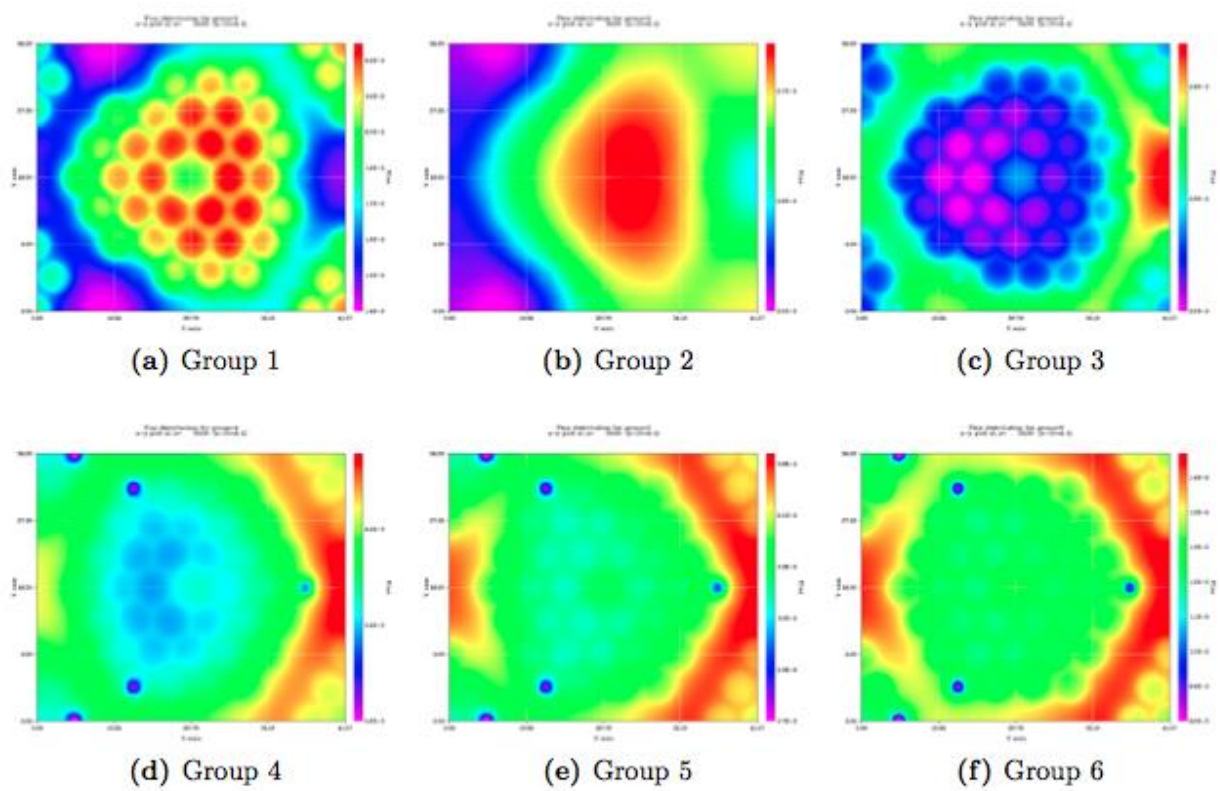

Figure 2.3.3: 6-group flux distribution calculated with PENTRAN.

The above flux distributions show expected physical behavior. For example, the group-1 flux show high values at the fuel rods, low values in water, and significant flux drop from the center rods to the boundary water region. Opposite behavior is observed for the lower energy groups, especially the 6th group which corresponds to thermal energy group.
We have performed a series of sensitivity studies for different combinations of spatial fine meshes and angular quadrature orders.

For spatial meshing we considered coarser meshing including, 30x30 and 40x40, and finer meshing 60x60 and 70x70. For angular discretization we considered lower quadrature orders of s4 and s8, and high quadrature orders of s16 and s20.
Figure compares root mean square (RMS) of energy weighted-average of 6-group flux distributions for different spatial and angular quadrature order combinations as compared to the most refined case with 70x70 meshes and quadrature order of S20.

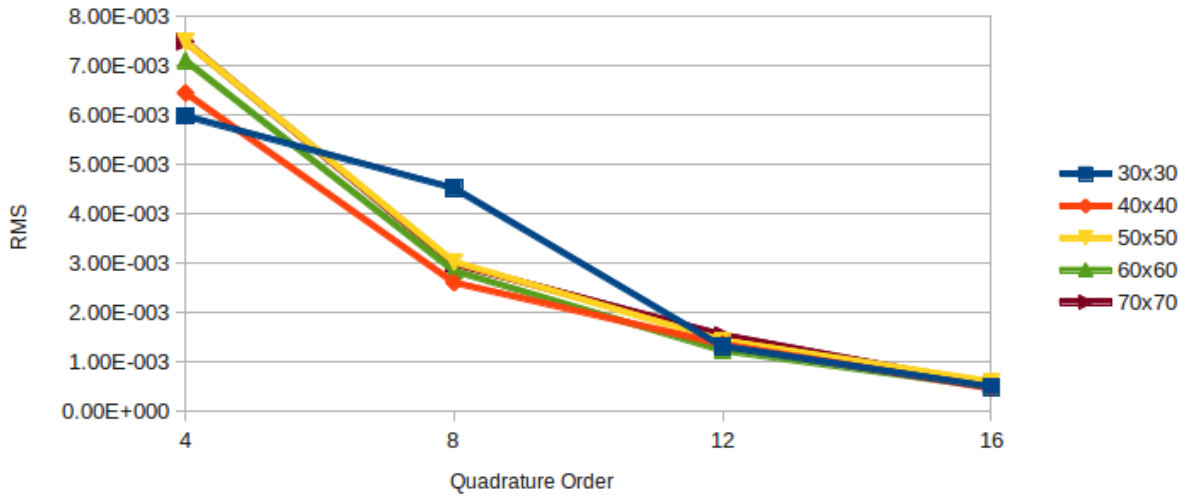

Figure 2.3.4: Comparison of flux differences, in RMS, as compared to the s20 quadrature set of the given mesh.

The above figure indicates that a combination of 50x50 fine meshes and S8 quadrature order yields sufficient precision as compared to higher quadrature orders. This is especially important considering the computation cost given in Table .

Table 2.3.3: PENTRAN computation times, in minutes, for different combinations of meshing and quadrature order.

Number	**Quadrature Order**				
FM/CM	**4**	**8**	**12**	**16**	**20**
30	5.5	16.7	34.0	58.5	915
40	10.3	28.7	60.9	90.4	162.7
50	16.3	46.5	98.7	128.3	262.7
60	21.8	69.9	142.0	245.3	370.4
70	31.7	87.8	192.5	279.8	498.7

The above table indicates that the case with sufficient precision, i.e., 50x50 and S8, is faster by one order of magnitude as compared with the case with the highest refinements of 70x70 and S20.
We also compare above calculations based on the two important integral quantities including eigenvalue and generated power in each fuel cell. Figure compares relative difference of eigenvalues, in pcm, for different PENTRAN cases as compared to the MCNP predictions.

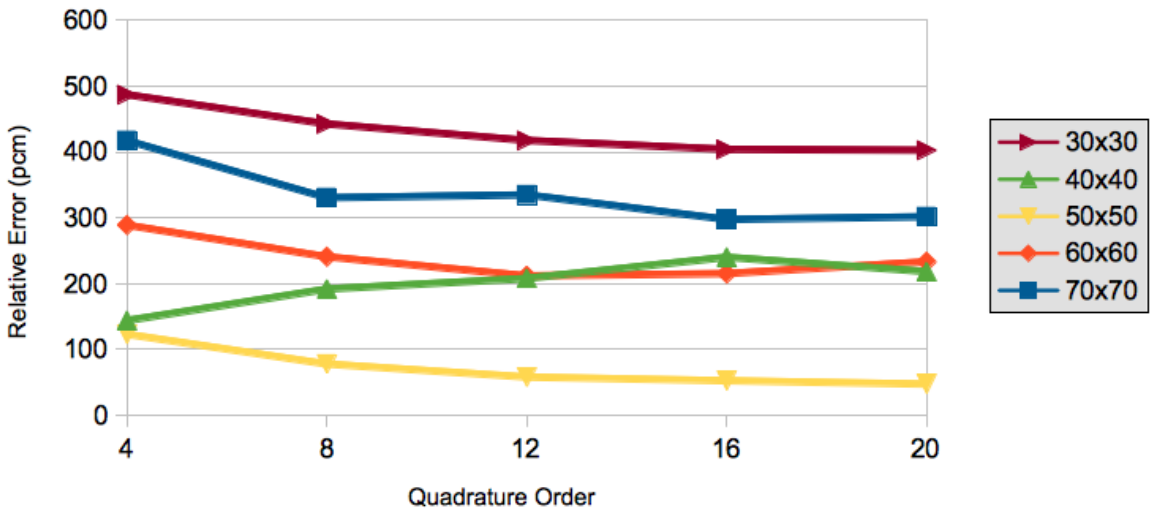

Figure 2.3.5: Relative difference, in pcm, of eigenvalues from PENTRAN calculations as compared to MCNP predictions.

The above figure indicates that using too fine of a mesh with too few direction will yield poor accuracy, as is seen in both the 60x60 and 70x70 fine mesh per coarse mesh cases. A good tradeoff is using the 50x50 fine meshes per coarse mesh case with an s8 or s12 quadrature set. By observing the increase in required computation time in going from s8 to s12, we consider that quadrature order of s8 is sufficient. Figure shows the relative errors of the average assembly power.

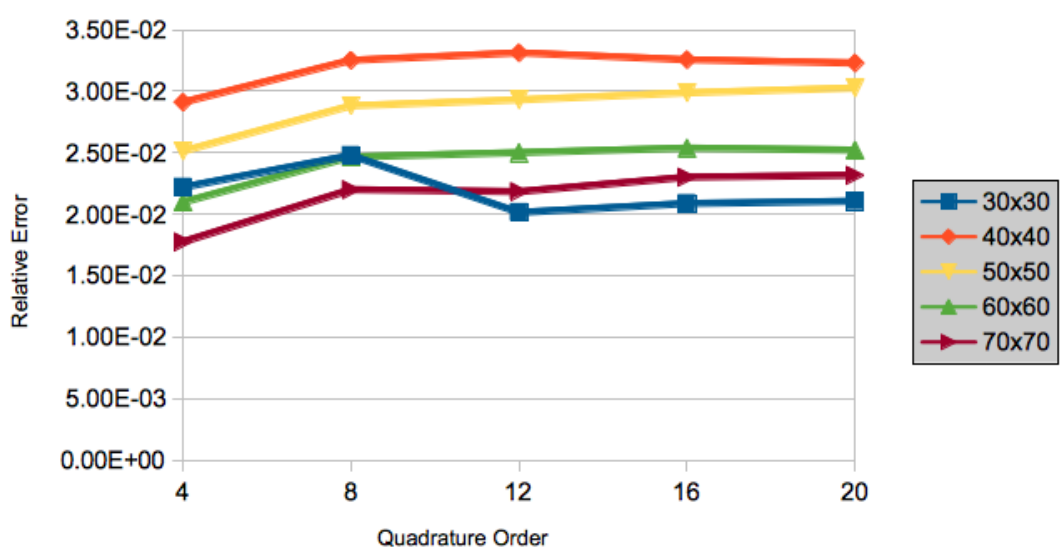

Figure 2.3.6: Relative difference in average assembly power for different combinations of meshing and quadrature order.

Considering the above diagram and previous information on flux and eigenvalue, it is evident that a PENTRAN model with 50x50 fine meshes and quadrature order of S8 is adequate for simulation of the HTTR fuel assembly.

Finally, we have examined the effect of different parallel decomposition methods including angular, spatial, and hybrid angular-spatial. In the following tables, all errors are calculated against the MCNP model solution. In each table the base case is marked with an asterisk (*). The base case has a meshing of 50x50 fine meshes per coarse mesh, P0 scattering order, S8 quadrature order, the model used system rebalance (SR) acceleration scheme, and is the simulation is controlled by a maximum of 15 inner iterations per outer iteration, and convergence tolerances of 10^{-5} for both *k*-eigenvalue and flux.
Table compares the solution accuracy and efficiency for different number of processors dedicated for angular decomposition.

Table 2.3.4: Performance of the PENTRAN calculations for different number of processors allocated for angular decomposition.

No. Proc	**No. Octant/proc**	**k**	**pcm**	**Time – [min.]**	**Speedup**
1	8	1.15062	40	228.3	1.00
2	4	1.15023	73	147.5	1.55
4	2	1.15031	66	84.9	2.69
8*	1	1.15018	78	46.4	4.92

The above table indicates as the number of processors increases, significant parallel speedups are achieved, while the solution accuracy remains relatively accurate. The reason for the observed difference between the parallel and serial cases can be attributed to the fact that the convergence criteria for the eigenvalue is set to 10^{-5}.
Table shows the effect of using different number of processors allocated for spatial decomposition only.

Table 2.3.5: Performance of PENTRAN calculations with different number of processors allocated for spatial decomposition.

No. Proc	**No. CM/proc**	**k**	**pcm**	**Time – [min.]**	**Speedup**
1	16	1.15062	40	289.6	1.00
2	8	1.15037	62	160.6	1.80
4	4	1.15007	87	84.9	3.41
8	2	1.15017	79	49.6	5.84
16	1	1.15053	47	24.5	11.82

The above table, Table , demonstrates that significant speedups can be achieved using spatial parallel decomposition while maintaining an acceptable level of solution accuracy. Again, the difference in eigenvalue may be attributed to the lower convergence criteria used.

The next parallel effect to examine is to examine hybrid space-angle parallel decomposition. The results displayed in Table , are for 2 processors dedicated to angular decomposition, and different number of processors for spatial decomposition. The number of processors in the first column refers to the total number of processors used. The speedups in this table are calculated as compared to the case with no parallel decomposition.

Table 2.3.6: Effect on PENTRAN calculations for different number of processors for hybrid space-angle decomposition.

No. Proc.*	**No. CM/proc**	**k**	**pcm**	**Time – [min.]**	**Speedup**
4	8	1.15022	74	82.6	2.76
8	4	1.15020	76	44.2	5.17
16	2	1.15010	85	36.5	6.26

*All cases use 2 processors for angular decomposition.

This table demonstrates that significant speedups can be achieved by decomposing the phase space both angularly and spatially, while still maintaining similar solution accuracy as previous decomposition cases. This leads to the conclusion that one should spatially decompose the problem before considering angular decomposition, especially in the case where a low order of angular discretization is used.

2.4 Implement the theory into the selected codes in 2D and solve 2D benchmarks

2.4.1 Geometry and Model Specifications

The SDM algorithm is tested on the 2D HTTR core test problem defined by Zhang et. al. [10]. There are 3 different materials used in the model with cross-section information from the 26-group HELIOS library. Model geometry specifications are presented in Figure .

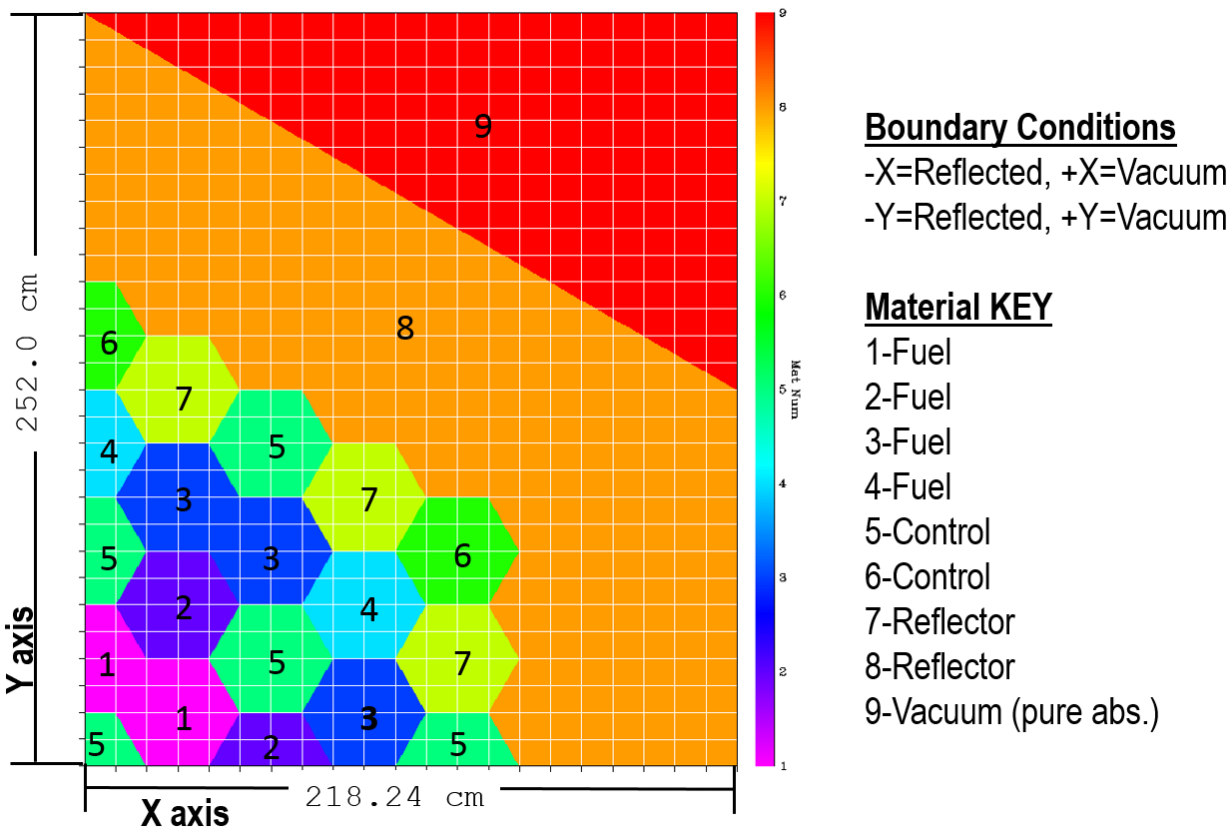

Figure 2.4.1: 2D HTTR core geometry, material layout, and boundary conditions.

The modeling parameters are shown in Table and meshing information is shown in Table .

Table 2.4.1: 2D HTTR modeling parameters.

Parameter	ID	Value
Scattering Order	legord	P0
Quadrature Order	oquad	s6
k-tolerance	tolout	1.0E–07
flux-tolerance[1]	tolicm	1.0E–05 (core) 1.0E–03 (refl.) 1.0E+00 (void)
Max. flux iters.	maxinn	10
Max. k iters	maxout	1000

[1]Regional flux tolerances were implemented.

Except for a lower quadrature order of S6, the remaining parameters are the same as were used for the 1-D calculations.

Table 2.4.2: 2D HTTR meshing information

Region	**Mesh Size**
Core	0.3 x *mfp*
Reflector	1.0 x *mfp*

The above meshing is based on material mean free paths (mfp). A given material's mean free path defined as the inverse of the maximum group total cross section. The void region is an artificially created material to simulate a vacuum boundary condition along the diagonal boundary, fine mesh dimensions in this region are 5.19 by 4.50cm.

2.4.2 2-D, 26-group Calculations

The 26-group calculation, using the parameters listed in Table , is used as the reference case. All calculations in this section are performed on a single processor. The keff and performance parameters for the reference case are given in Table .

Table 2.4.3: Keff and performance parameters for the 2-D multigroup reference case.

k_{eff}	Iterations[1]	Time - [hrs]
1.04472	271	11.3

[1]Total number of k (Outer) iterations.

Figure presents fast, groups 1-17, and thermal, groups 18-26, flux distributions for the 2-D, 26-group calculation.

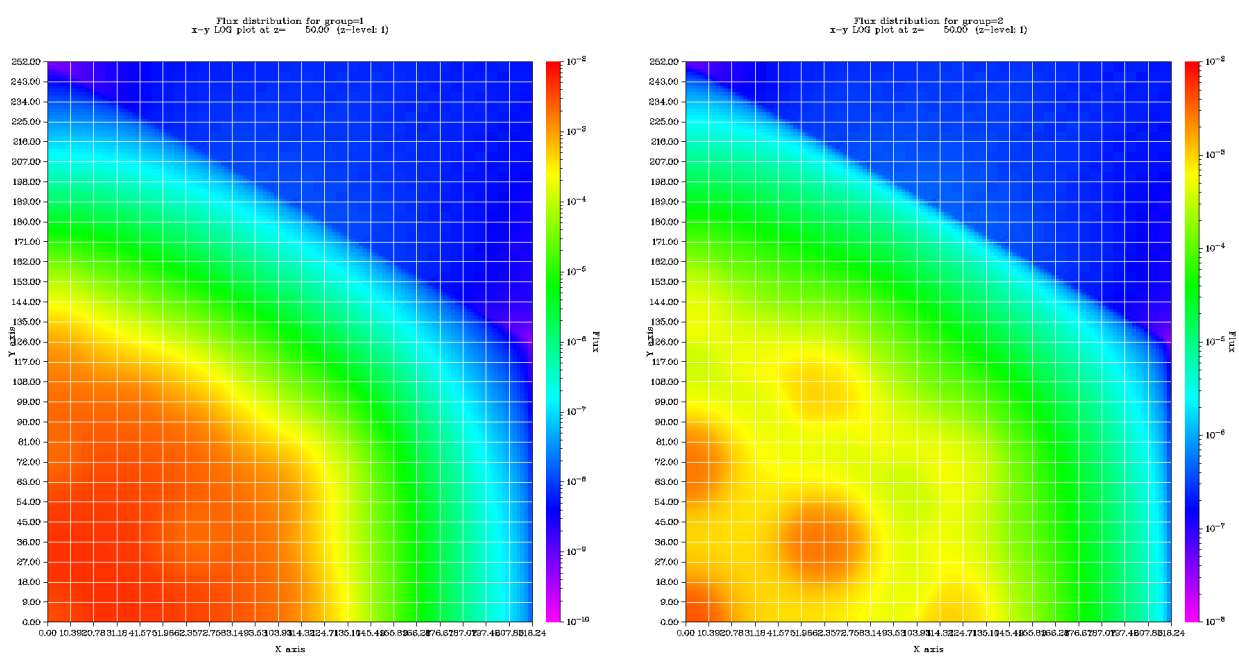

(a) Fast. (b) Thermal.

Figure 2.4.2: 26-group reference case flux distribution.

Above diagrams demonstrate expected behavior, i.e., fast flux shows exponential drop from core center to its periphery, and thermal shows expected high and low values depending on the material regions.
To examine the physical behavior of flux distributions in Figure we show horizontal (a) profiles of fast and thermal fluxes, and we show vertical profiles (b) of the fast and thermal fluxes.

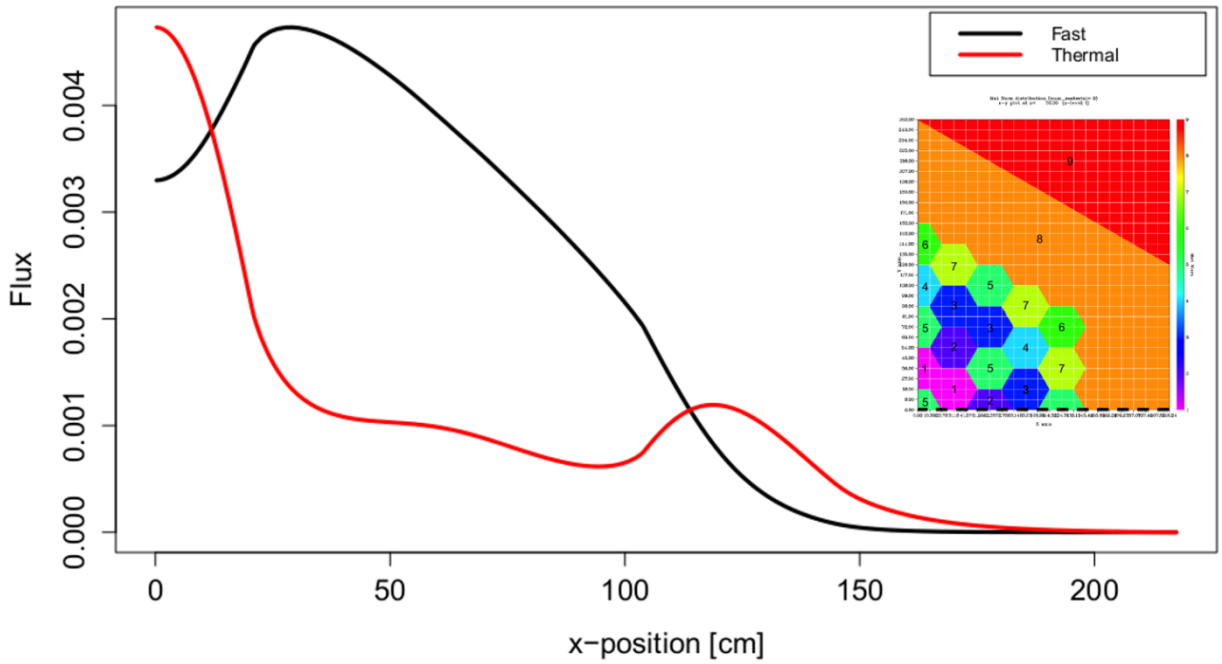

(a) Horizontal slice at y=0.0cm.

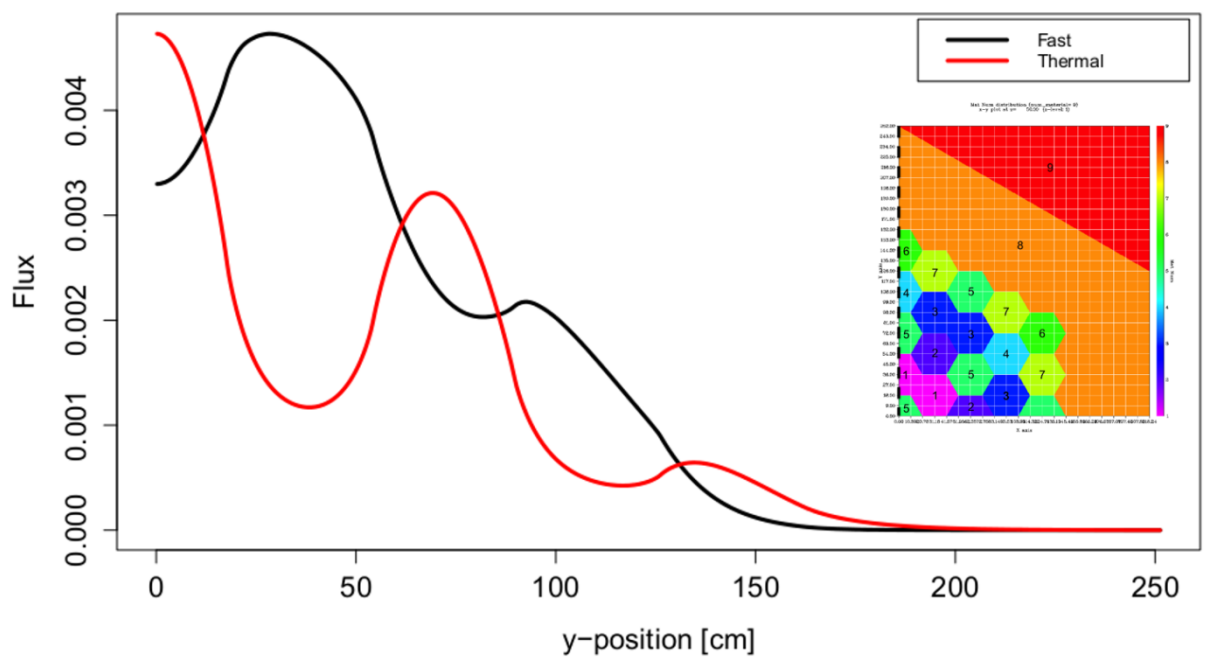

(b) Vertical slice at x=0.0cm.

Figure 2.4.3: Comparison of profiles of 2-D flux distributions for the reference multigroup calculation.

Again, above diagrams demonstrate the expected behavior that is fast and thermal fluxes behave oppositely as the fast neutrons are scattered into thermal energies and thermal neutrons are absorbed in the fuel and control elements.

2.4.3 SDM Testing in 2-D model Parameters

The specific tolerances required for running the SDM algorithm for the 2D homogenized HTTR core are listed in Table . The same meshing, scattering order, and quadrature order are used as specified for the 26-group reference case, Table and Table .

Table 2.4.4: 2D HTTR SDM modeling parameters.

Parameter	ID	Value
k-tolerance	`tolout`	1.0E–06
flux-tolerance[1]	`tolicm`	1.0E–05 (core) 1.0E–03 (refl.) 1.0E+00 (void)
CG cross section tol.	`tolsgr`	1.0E-01
FG flux tol.	`tolfgr`	1.0E+00
Max. CG flux iters.	`maxinn`	10
Max. CG k iters	`maxout`	20
Max. subgroup iters	`maxsgr`	200

[1]Regional flux tolerances were implemented.

2.4.4 Coarse-group Testing Structure

Table shows the coarse-group structures considered for examining the SDM algorithm in 2-D. Note that again the number given for each group structure correspond fine group ID which corresponds to the lower boundary of the corresponding coarse group.

Table 2.4.5: SDM coarse-group testing structure.

Test Case	Coarse-Group ID #												
	1	2	3	4	5	6	7	8	9	10	11	12	13
	Fine-Group ID # (Lower Energy Bound)												
2cg	17	26											
3cg	6	17	26										
5cg	6	12	17	21	26								
6cg	3	6	12	17	21	26							
4cg-Fast	3	6	17	26									
4cg-Epi	6	12	17	26									
4cg-Thrm	6	17	21	26									
8cg-Epi	3	6	9	12	15	17	21	26					
8cg-Thrm	3	6	12	17	19	21	24	26					
10cg-Epi	3	6	8	10	12	14	16	18	21	26			
13cg-Thrm	3	6	12	17	18	19	20	21	22	23	24	25	26

To select the above coarse group structures, we considered similar approach as discussed for the 47-group structure. More specifically, the cross sections were plotted versus energy groups and the trends were examined to determine appropriate bounds for the fast, epithermal, and thermal energy ranges. These selections were chosen by an informed decision, not by the actual value of the energy level that defines group bounds (this information was not available). Again, just like the 47-group case, the coarse-group structures were decided on by independently refining the different energy regions- fast, epithermal, and thermal.

2.4.5 SDM Testing Results

The keff and performance parameters for the different SDM coarse-group calculations are presented in Table . Again, k-eff errors are presented in percent mili reactivity (pcm), speedups are defined as (time of reference solution)/(time of SDM solution), and maximum percent flux errors are calculated for fast and thermal fluxes within the fuel regions and overall, in the whole core.

Table 2.4.6: Summary of results of the SDM of the 2D homogenized HTTR core.

	k_{eff}	pcm[1]	SG[2] Iters	CG[3] Iters	Speedup	Flux Error[4] Fuel Region	Flux Error[4] Reflector
26g-Ref	1.04472	ref.	n/a	271	1.00	ref.	ref.
2cg	1.04482	10	80	1077	1.08	0.26	6.1
3cg	1.04480	8	33	475	2.05	0.24	6.2
5cg	1.04490	17	21	288	2.44	0.28	6.5
6cg	1.04479	7	24	263	2.24	0.37	7.0
8cg-Epi	1.04483	11	30	328	1.63	0.35	6.9
10cg-Epi	1.04478	6	25	390	1.45	0.29	6.2
8cg-Thrm	1.04480	8	29	303	1.66	0.21	5.5
13cg-Thrm	1.04464	-8	16	252	1.21	0.12	0.5

[1]per cent mili reactivity error; [2]subgroup; [3]coarse-group; [4]maximum absolute flux error

Table shows that all group structures are in good agreement for eigenvalue and flux in the fuel region, under +/-20pcm and under 0.4% error, respectively. Here the maximum errors occurred in the void region, outside of the reflector; these errors remain under 7%. These errors may seem large, but they have very little effect on the solution because they are so far away from the fuel region.

Speedups for the 2D homogenized core are not as large as those for the 1D core. With the 5cg structure a speedup of 2.44 is observed, which considering that the reference model makes over 11 hours to complete a speedup greater than 2 is quite significant. Again here it can be seen that the coarse-group arrangement affects the computation time; choosing too few or too many groups will cause slower convergence. Figure shows the 2D flux error distributions, comparing the 6-group case with the reference 26-group case.

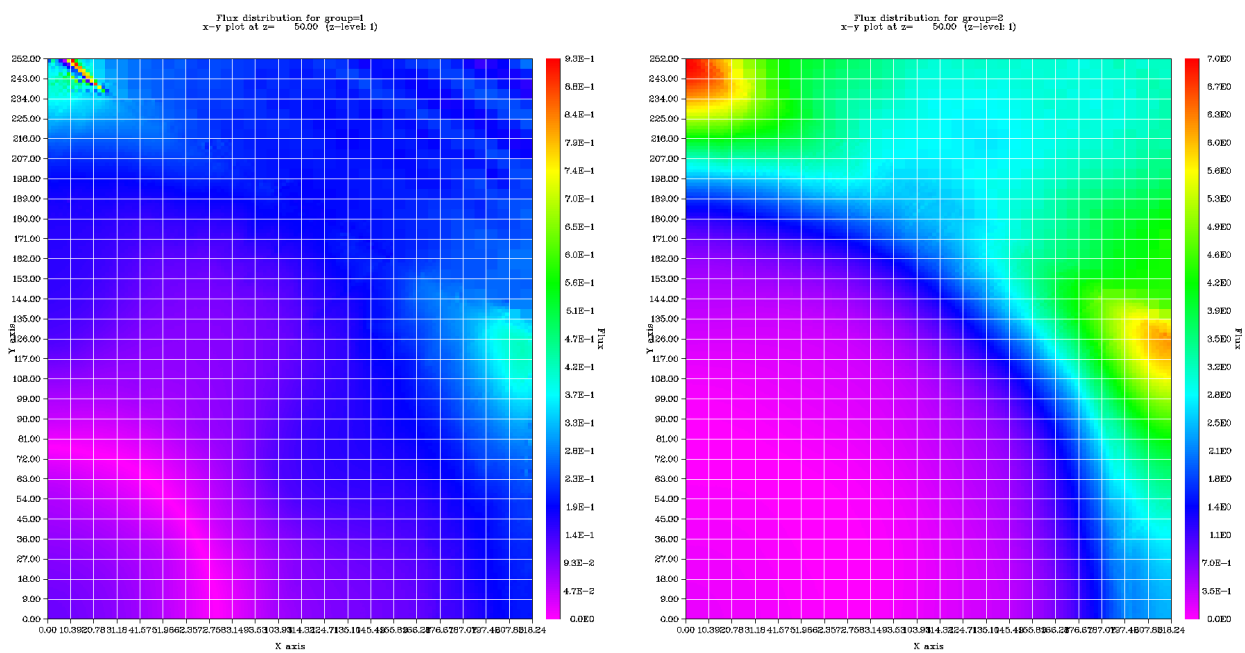

(a) Fast. (b) Thermal.

Figure 2.4.4: 6cg flux error distribution.

It appears that differences are less than 1.0% in core and reflector. The larger errors are in the void, which is not important, as it is an artificial region for representing a hexagonal model with a Cartesian geometry. It is also important to note that above diagrams show absolute values of the errors. The zero line differentiates the positive and negative errors, i.e., where the flux errors go from positive to negative, moving from the core to the reflector. This effect is better observed by viewing the 1D flux error profiles of Figure .

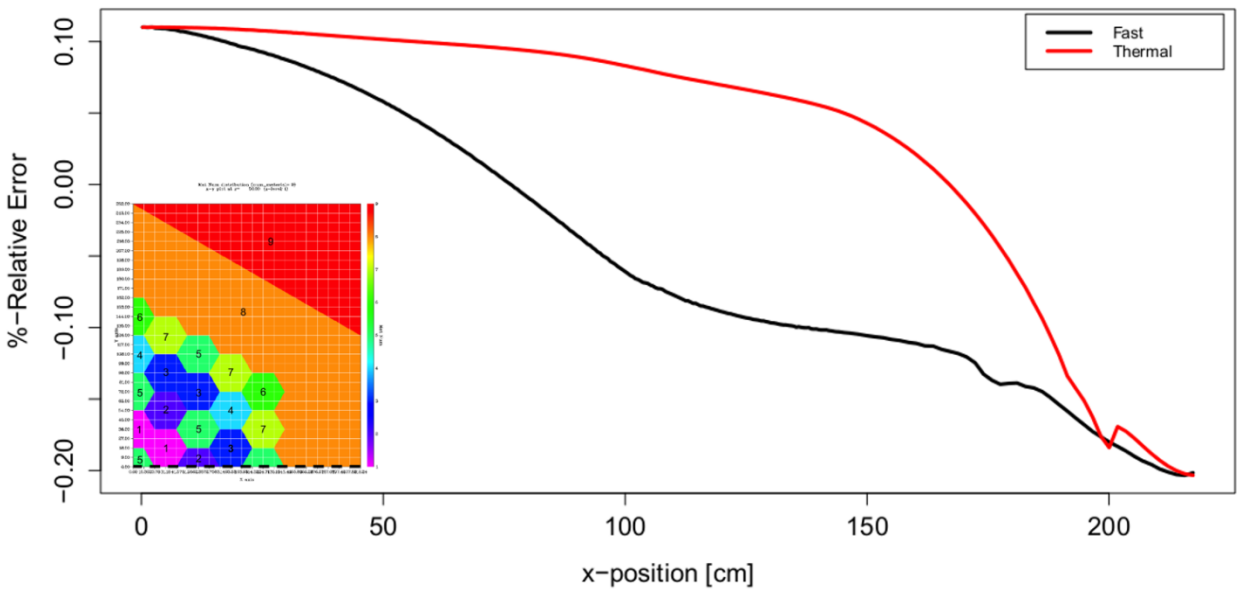

(a) Horizontal slice at y=0.0cm.

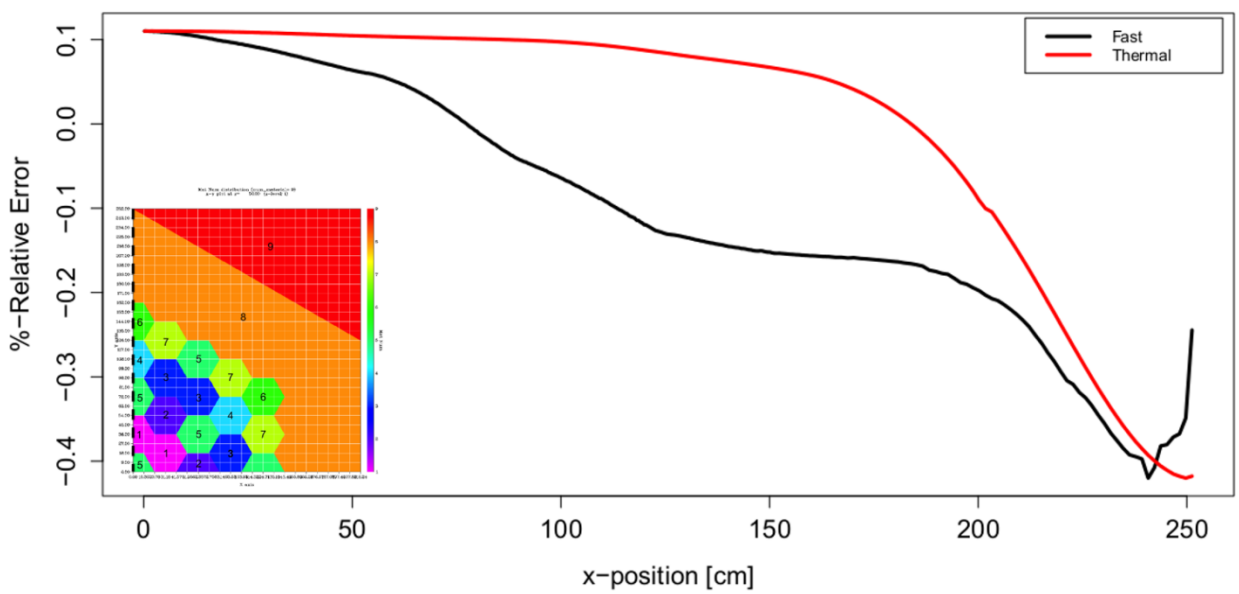

(b) Vertical slice at x=0.0cm.

Figure 2.4.5: 26-group reference 1D flux error profiles.

The 1D flux error profiles in Figure show much more clearly how the flux error transitions from negative to positive when moving from the fuel region to the reflector. It also shows that the maximum error is occurring out in the reflector region.

Task 2.5 Explore a 1D diffusion approximation for the new multi-group theory

Consider an eigenvalue fine-group diffusion equation with G number of energy bins $\{g \mid g=1, 2, 3,\ldots, G\}$ as shown in Eq. (2.5.1):

$$\nabla.J^g(\vec{r}) + \sigma_{re}^g(\vec{r})\phi^g(\vec{r}) = \sum_{g'=1}^{G} \sigma_{s,re}^{g'\to g}(\vec{r})\phi^{g'}(\vec{r}) + \frac{\chi^g}{k}\sum_{g'=1}^{G} \nu\sigma_f^{g'}(\vec{r})\phi^{g'}(\vec{r})$$
$$J^g(\vec{r}) = -D^g(\vec{r})\nabla\phi^g(\vec{r}) = -\frac{1}{3\sigma_{tr}^g(\vec{r})}\nabla\phi^g(\vec{r}) \tag{2.5.1}$$

where the fission term is assumed isotropic with removal and transport cross sections defined as:

$$\sigma_{re}^g = \sigma^g - \sigma_s^{g\to g} \tag{2.5.2}$$

$$\sigma_{s,re}^{g'\to g} = \begin{cases} \sigma_s^{g'\to g} & if\ g' \neq g \\ 0 & if\ g' = g \end{cases} \tag{2.5.3}$$

and

$$\sigma_{tr}^g = \sigma^g - \sigma_{s1}^g = \sigma_a^g + (1-\bar{\mu}^g)\sigma_s^g \tag{2.5.4}$$

It should be noted the principle of detailed balance, i.e., Eq. (2.5.5), has been implicitly applied to Eq. (2.5.1) which is a common approximation for multi-group diffusion equation.

$$\sum_{g'=1}^{G} \sigma_{s1}^{g'\to g} J^{g'} \cong \sum_{g'=1}^{G} \sigma_{s1}^{g\to g'} J^g = \sigma_{s1}^g J^g \tag{2.5.5}$$

Let C be the number of coarse groups where any fine-group *h* is fully contained in coarse-group *c*. In accordance with the reference work [13], the fine-group *h* is referred to as a "subgroup" of a coarse-group in which it is contained. The coarse-group diffusion/P_1 equation is defined by starting from the fine-group transport equation, integrating/summing over the energy range contained in coarse-group *c* and taking the 0th and 1st angular moment of the coarse-group transport equation assuming coarse-group flux is linearly anisotropic.

To be consistent with the fine-group diffusion equation in Eq. (2.5.1), the cross sections (total and scattering) in fine-group transport equation are transport corrected and fission term is assumed isotropic. The resulting transport equation is shown in Eq. (2.5.6).

$$\hat{\Omega}.\nabla\psi^h(\vec{r},\hat{\Omega}) + \sigma_{tr}^h(\vec{r})\psi^h(\vec{r},\hat{\Omega})$$
$$= \sum_{h'=1}^{G} \int_{4\pi} d\hat{\Omega}' \frac{\tilde{\sigma}_s^{h'\to h}(\vec{r})}{4\pi}\psi^{h'}(\vec{r},\hat{\Omega}') + \frac{\chi^h}{4\pi k}\sum_{h'=1}^{G} \nu\sigma_f^{h'}(\vec{r})\phi^{h'}(\vec{r}) \tag{2.5.6}$$

where transport corrected cross sections are defined in Eqs. (2.5.7) and (2.5.8).

$$\sigma_{tr}^{h} = \sigma^{h} - \sigma_{s1}^{h} = \sigma_{a}^{h} + (1 - \bar{\mu}^{h})\sigma_{s}^{h} \tag{2.5.7}$$

$$\tilde{\sigma}_{s}^{h'\to h} = \begin{cases} \sigma_{s}^{h'\to h} & if\ h' \neq h \\ \sigma_{s}^{h'\to h} - \sigma_{s1}^{h} = \sigma_{s}^{h'\to h} - \bar{\mu}^{h}\sigma_{s}^{h} & if\ h' = h \end{cases} \tag{2.5.8}$$

The coarse-group transport equation is obtained by summing over the fine groups within group c as shown below.

$$\begin{aligned} \hat{\Omega}.\nabla\psi^{c}(\vec{r},\hat{\Omega}) + \sigma_{tr}^{c}(\vec{r})\psi^{c}(\vec{r},\hat{\Omega}) \\ = \sum_{c'=1}^{C} \int_{4\pi} d\hat{\Omega}' \frac{\tilde{\sigma}_{s}^{c'\to c}(\vec{r})}{4\pi}\psi^{c'}(\vec{r},\hat{\Omega}') + \frac{\chi^{c}}{4\pi k^{c}} \sum_{c'=1}^{C} \nu\sigma_{f}^{c'}(\vec{r})\phi^{c'}(\vec{r}) \\ + \delta^{c}(\vec{r},\hat{\Omega})\phi^{c}(\vec{r}) \end{aligned} \tag{2.5.9}$$

where the coarse-group coefficients are defined in the following equations.

$$\psi^{c}(\vec{r},\hat{\Omega}) = \sum_{h\in c} \psi^{h}(\vec{r},\hat{\Omega}) \tag{2.5.10}$$

$$\sigma_{tr}^{c}(\vec{r}) = \frac{\sum_{h\in c} \sigma_{tr}^{h}(\vec{r})\phi^{h}(\vec{r})}{\sum_{h\in c} \phi^{h}(\vec{r})} \tag{2.5.11}$$

$$\tilde{\sigma}_{s}^{c'\to c}(\vec{r}) = \frac{\sum_{h\in c}\sum_{h'\in c'} \tilde{\sigma}_{s}^{h'\to h}(\vec{r})\phi^{h'}(\vec{r})}{\sum_{h'\in c'} \phi^{h'}(\vec{r})} \tag{2.5.12}$$

$$\chi^{c} = \sum_{h\in c} \chi^{h} \tag{2.5.13}$$

$$\nu\sigma_{f}^{c'}(\vec{r}) = \frac{\sum_{h'\in c'} \nu\sigma_{f}{}^{h'}(\vec{r})\phi^{h'}(\vec{r})}{\sum_{h'\in c'} \phi^{h'}(\vec{r})} \tag{2.5.14}$$

and

$$\delta^{c}(\vec{r},\hat{\Omega}) = \frac{\sum_{h\in c}[\sigma_{tr}^{c}(\vec{r}) - \sigma_{tr}^{h}(\vec{r})]\psi^{h}(\vec{r},\hat{\Omega})}{\sum_{h\in c} \phi^{h}(\vec{r})} \tag{2.5.15}$$

The 0th and 1st angular moments of Eq. (2.5.9) are derived by assuming linearly anisotropic coarse-group flux as shown in Eq. (2.5.16).

$$\nabla.J^c(\vec{r}) + \sigma_{tr}^c(\vec{r})\phi^c(\vec{r}) = \sum_{c'=1}^{C} \tilde{\sigma}_s^{c'\to c}(\vec{r})\phi^{c'}(\vec{r}) + \frac{\chi^c}{k^c}\sum_{c'=1}^{C} \nu\sigma_f^{c'}(\vec{r})\phi^{c'}(\vec{r}) + \int_{4\pi} d\hat{\Omega}\, \delta^c(\vec{r},\hat{\Omega})\phi^c(\vec{r})$$
$$\frac{1}{3}\nabla\phi^c(\vec{r}) + \sigma_{tr}^c(\vec{r})J^c(\vec{r}) = \int_{4\pi} d\hat{\Omega}\,\hat{\Omega}\delta^c(\vec{r},\hat{\Omega})\phi^c(\vec{r}) \tag{2.5.16}$$

Using Eq. (2.5.15), the coarse group P_1 equation is simplified to:

$$\nabla.J^c(\vec{r}) + \sigma_{tr}^c(\vec{r})\phi^c(\vec{r}) = \sum_{c'=1}^{C} \tilde{\sigma}_s^{c'\to c}(\vec{r})\phi^{c'}(\vec{r}) + \frac{\chi^c}{k^c}\sum_{c'=1}^{C} \nu\sigma_f^{c'}(\vec{r})\phi^{c'}(\vec{r})$$
$$\frac{1}{3}\nabla\phi^c(\vec{r}) + \sigma_{tr}^c(\vec{r})J^c(\vec{r}) = \delta_1^c(\vec{r})\phi^c(\vec{r}) \tag{2.5.17}$$

where δ_1^c is defined as:

$$\delta_1^c(\vec{r}) = \frac{\sum_{h\in c}[\sigma_{tr}^c(\vec{r}) - \sigma_{tr}^h(\vec{r})]J^h(\vec{r})}{\sum_{h\in c}\phi^h(\vec{r})} \tag{2.5.18}$$

δ_1^c is a "perturbation cross section" that is required to maintain the consistency of the coarse-group P_1 equations with fine-group diffusion and it is commonly omitted from coarse-group diffusion calculation. It is worth noting that one might consider further simplifying Eq. (2.5.17) to remove the in-group scattering cross section from the total cross section. However, for coarse-group calculations using standard power iteration scheme this might result in numerical instabilities and/or longer convergence time. Thus for this report, Eq. (2.5.17) is used for coarse-group P_1 calculations.

In order to unfold the fine-group flux from the coarse-group solution, a "decomposition sweep" is required. In this process, fine-group diffusion is solved where the source term for any subgroup *h* is modified to take into account the newly calculated coarse-group flux. To this extent, the reaction rates (scattering and fission) in any subgroup *h* are represented through "subgroup decomposition cross sections" multiplied by respective coarse-group fluxes. The subgroup decomposition cross sections are calculated in the same manner as those found in Eqs. (2.5.10)- (2.5.15). Hence, the fine-group diffusion decomposition sweep is defined as:

$$-\nabla.D^h(\vec{r})\nabla\phi^h(\vec{r}) + \sigma_{re}^h(\vec{r})\phi^h(\vec{r}) = \sum_{c'=1}^{C} \sigma_{s,re}^{c'\to h}(\vec{r})\phi^{c'}(\vec{r}) + \frac{1}{k^c}\sum_{c'=1}^{C} \chi^h\nu\sigma_f^{c'}(\vec{r})\phi^{c'}(\vec{r}) \tag{2.5.19}$$

where the subgroup decomposition cross sections are:

$$\sigma_{s,re}^{c'\to h}(\vec{r}) = \frac{\sum_{h'\in c'}\sigma_{s,re}^{h'\to h}(\vec{r})\phi^{h'}(\vec{r})}{\sum_{h'\in c'}\phi^{h'}(\vec{r})} \tag{2.5.20}$$

$$\chi^h \nu\sigma_f^{c'}(\vec{r}) = \frac{\chi^h \sum_{h'\in c'} \nu\sigma_f{}^{h'}(\vec{r})\phi^{h'}(\vec{r})}{\sum_{h'\in c'} \phi^{h'}(\vec{r})} \tag{2.5.21}$$

The decomposition sweep is computationally cheap since its cross sections are already computed from the flux guess and the coarse-group flux and eigenvalue are calculated by solving Eq. (2.5.17). Therefore, no source iteration is involved and all terms on the RHS of Eq. (2.5.19) are known quantities.

As explained, the cross sections in Eqs. (2.5.17) are dependent on the initial fine-group flux. If the fine-group flux guess is the solution to the fine-group diffusion equation, the coarse-group flux is consistent with the fine-group solution and only one decomposition sweep is required to unfold the detailed flux spectrum. However, this is not the case in practice and a recondensation procedure is necessary to incorporate the correct core environment in the initial spectrum obtained by assembly calculations with approximate boundary conditions. The recondensation procedure is comprised of solving Eqs. (2.5.17) and (2.5.19) iteratively and using the solution of Eq. (2.5.19) as a new subgroup flux guess. Nonetheless, this scheme would be unstable for most problems and would not lead to a converged solution. Therefore, an additional step is added to stabilize the recondensation procedure. Two "stabilizing schemes" are presented.

The first stabilizing scheme, core sweeping, is similar to that developed in [13]. During core sweeping, a single diffusion sweep for each subgroup is carried out where the multi-group flux with subscript "*p*" is the solution to Eq. (2.5.19) and k^c is the coarse-group eigenvalue from Eq. (2.5.17). The updated flux is denoted with subscript "*p+1/2*". The subscript refers to the number of times the coarse-group diffusion is solved and the flux update is performed to correct for the core environment. Therefore, subscript *p+1/2* refers to an intermediate step between *p* and *p+1* where the stabilization is performed to ensure convergence.

$$\begin{aligned} -\nabla.D^h(\vec{r})\nabla\phi_{p+1/2}^h(\vec{r}) + \sigma_{re}^h(\vec{r})\phi_{p+1/2}^h(\vec{r}) \\ = \sum_{h'=1}^{G} \sigma_{s,re}^{h'\to h}(\vec{r})\phi_p^{h'}(\vec{r}) + \frac{\chi^h}{k^c}\sum_{h'=1}^{G} \nu\sigma_f^{h'}(\vec{r})\phi_p^{h'}(\vec{r}) \end{aligned} \tag{2.5.22}$$

The second stabilizing scheme is an embedded assembly level fixed source diffusion calculation. During this scheme, a fixed source problem at the assembly level is solved using the coarse-group eigenvalue from Eq. (2.5.17) and incoming currents calculated from the solution of Eq. (2.5.19) at the interface of the assemblies.

$$\begin{aligned} -\nabla.D^h(\vec{r})\nabla\phi_{p+1/2}^h(\vec{r}) + \sigma_{re}^h(\vec{r})\phi_{p+1/2}^h(\vec{r}) \\ = \sum_{h'=1}^{G} \sigma_{s,re}^{h'\to h}(\vec{r})\phi_{p+1/2}^{h'}(\vec{r}) + \frac{\chi^h}{k^c}\sum_{h'=1}^{G} \nu\sigma_f^{h'}(\vec{r})\phi_{p+1/2}^{h'}(\vec{r}) \end{aligned} \tag{2.5.23}$$

The boundary condition for the fixed source diffusion problem is defined in Eq. (2.5.24).

$$
\begin{aligned}
J(\vec{r}_s)^h_{inc,p} &= \hat{n}_s . \int_{2\pi^-} d\hat{\Omega}\, \hat{\Omega} \psi^h_{p+1/2}(\vec{r}_s, \hat{\Omega}) \\
&= \hat{n}_s . \int_{2\pi^-} d\hat{\Omega}\, \hat{\Omega} \left\{ \frac{1}{4\pi} \phi(\vec{r}_s)^h_{p+\frac{1}{2}} + \frac{3}{4\pi} \hat{\Omega} . \vec{J}(\vec{r}_s)^h_{p+\frac{1}{2}} \right\} \\
&= \frac{1}{4} \phi(\vec{r}_s)^h_{p+\frac{1}{2}} + \frac{D^h(\vec{r})}{2} \hat{n}_s . \nabla \phi(\vec{r}_s)^h_{p+\frac{1}{2}}
\end{aligned}
\tag{2.5.24}
$$

Regardless of the stabilizing scheme performed, the updated flux is used as a fine-group flux guess for the next iteration. In summary, the recondensation scheme is described as below.

1. Perform fine-group assembly calculations with approximate boundary conditions to generate the initial flux spectrum and apply this spectrum to Eqs. (2.5.11)-(2.5.14), (2.5.18), (2.5.20) and (2.5.21) to generate coarse-group and decomposition cross sections.
2. Solve the coarse-group whole-core diffusion equation using the cross sections generated in step (1).
3. Perform a diffusion decomposition sweep for each subgroup using the decomposition cross sections generated in step (1) with the coarse-group eigenvalue and scalar flux in step (2).
4. Perform the stabilizing scheme (i.e., core sweeping or assembly level fixed source calculations) using the subgroup flux obtained from step (3). The updated fine-group flux spectrum, i.e., ψ^g_{p+1} is used to update the coarse-group and decomposition cross sections.
5. Repeat steps (2) - (4) until the user defined successive iteration criteria for coarse-group flux and eigenvalue of Eqs. (2.5.25) and (2.5.26) are met where the subscript "p" is the iteration number.

$$
\left| \frac{\phi^c_{p+1}(\vec{r}) - \phi^c_p(\vec{r})}{\phi^c_{p+1}(\vec{r})} \right|_{max} < (\varepsilon_\phi)_{re-cond} \tag{2.5.25}
$$

and

$$
\left| \frac{k^c_{p+1} - k^c_p}{k^c_{p+1}} \right|_{max} < (\varepsilon_k)_{re-cond} \tag{2.5.26}
$$

Task 2.6 Expert Review of the status of the project

The project review was completed by Dr. Barry Ganapol of Arizona St. University on November 14, 2011.The report of his review was submitted into the NEUP program in our Y2Q3 report.

Task 3.1 Extend the Numerical Formulation to 3D

3.1.1 Formulations of 3D Deterministic Transport in Cartesian Geometry

In this section, we will discuss derivation of a SDM algorithm for the TITAN code [14] and elaborates on its implementation into TITAN.

This effort constitutes the adaptation of the Subgroup Decomposition Method (SDM) [13] in 3-D Cartesian Geometry. The SDM method extends the cross-section condensation process, preserving spectral accuracy in condensed-group transport using a direct coupling of consistent coarse-group criticality calculations with fixed-source ‘‘decomposition sweeps’’ to obtain the fine-group spectrum. This work documents an extension of the discrete ordinates 1-D work to fully consistent 3-D Cartesian geometry.

The 3-D implementation of the SDM requires a significant amount of added memory and computational operations to implement, as evident in the discussion below. Originally, plans were to modify the PENTRAN 3-D parallel Sn code; however, the larger memory requirements of SDM, coupled with the complexities of parallel execution among angle, energy, and space, made it simpler to adapt the SDM formulations into the TITAN 3-D code (serial version). As a result, testing has been performed with the TITAN code.

In steady state, the multi-group transport equation is [2]; the left side includes loss by leakage and collision, and scatter, fission, and independent sources are on the right:

$$\hat{\Omega}\cdot\nabla\psi_g(\vec{r},\hat{\Omega})+\sigma_g(\vec{r})\psi_g(\vec{r},\hat{\Omega})= \\ \sum_{g'=1}^{g}\int_{4\pi}d\Omega'\sigma_{s\,g'\to g}(\vec{r},\hat{\Omega}'\cdot\hat{\Omega})\psi_g(\vec{r},\hat{\Omega}')+\frac{\chi_g}{k_o}\sum_{g'=1}^{G}\int_{4\pi}d\Omega'\nu\sigma_{f\,g'}(\vec{r})\psi_{g'}(\vec{r},\hat{\Omega})+q_{ind\,g}(\vec{r},\hat{\Omega}) \tag{3.1.1}$$

Note that the angular variable is normalized on the unit sphere in the above formulation, so that integration over Ω is expressed in terms of the polar angle cosine μ and azimuthal angle ϕ as:

$$\int_{4\pi}d\Omega=\int_{-1}^{1}\frac{d\mu}{2}\int_{0}^{2\pi}\frac{d\varphi}{2\pi}=1 \tag{3.1.2}$$

Hereafter, this is implicitly assumed. The scattering term is then expanded using a truncated set of spherical (surface) harmonics, with $\hat{\Omega}\to<\theta,\phi>,\ \ (\hat{\Omega}'\ \cdot\hat{\Omega})\to(\mu_o),\ \ \mu=(\cos\theta),\ \ \mu'=(\cos\theta')$:

$$\sigma_{s\,g'\to g}(\vec{r},\mu_o)=\sum_{l=0}^{L}(2l+1)\sigma_{s\,g'\to g,l}(\vec{r})P_l(\mu_o) \tag{3.1.3}$$

$$\sigma_{s\,g'\to g,l}(\vec{r})=\int_{-1}^{1}\frac{d\mu_o}{2}\sigma_{s\,g'\to g}(\vec{r},\mu_o)P_l(\mu_o) \tag{3.1.4}$$

$$\mu_o=\mu\mu'+(1-\mu^2)^{1/2}(1-\mu'^2)^{1/2}\cos(\varphi-\varphi') \tag{3.1.5}$$

The Legendre polynomial $P_l(\mu_o)$, using the Legendre Addition Theorem, is:

$$P_l(\mu_o)=\frac{1}{(2l+1)}\sum_{k=-l}^{l}Y_{l,k}^{*}(\theta',\varphi')Y_{l,k}(\theta,\varphi) \tag{3.1.6}$$

The spherical (surface) harmonics $Y_{l,k}$ and $Y_{l,k}^{*}$ are defined in terms of the Associated Legendre polynomials and an exponential term:

$$Y_{l,k}(\theta,\varphi) = \sqrt{(2l+1)\frac{(l-k)!}{(l+k)!}} P_l^k(\mu)\exp(ik\varphi) \tag{3.1.7}$$

$$Y_{l,-k}(\theta,\varphi) = (-1)^k Y_{l,k}^{*}(\theta,\varphi) \tag{3.1.8}$$

Using Eqs.(3.1.5),(3.1.6), and (3.1.7), $P_l(\mu_0)$ can be written:

$$P_l(\mu_o) = P_l(\mu)P_l(\mu') + 2\sum_{k=1}^{l}\frac{(l-k)!}{(l+k)!}P_l^k(\mu)P_l^k(\mu')\cos(k(\varphi-\varphi')) \tag{3.1.9}$$

By trigonometric identity:

$$\cos(k(\varphi-\varphi')) = \cos(k\varphi)\cos(k\varphi') + \sin(k\varphi)\sin(k\varphi') \tag{3.1.10}$$

The vectors $\hat{\Omega} \rightarrow < \theta,\phi >$ on the unit sphere can be expressed as a set of direction cosines projected parallel to the *x*, *y*, and *z* axes, respectively, as $< \mu,\eta,\xi >$ Note that η and ξ can be expressed in terms of polar angle cosine μ and the azimuthal angle ϕ :

$$\eta = \sqrt{1-\mu^2}\cos(\varphi) \tag{3.1.11}$$

$$\xi = \sqrt{1-\mu^2}\sin(\varphi) \tag{3.1.12}$$

A 3-D Cartesian geometry (using a right handed coordinate system) is shown in Figure .

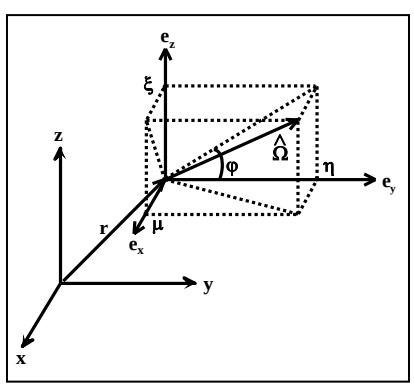

Figure 3.1.1: 3D Cartesian Geometry

If the streaming operator $\hat{\Omega}\cdot\nabla$ in Eq. 3.1.1 is expanded in 3-D Cartesian coordinates, it becomes:

$$\hat{\Omega}\cdot\nabla = \mu\frac{\partial}{\partial x} + \eta\frac{\partial}{\partial y} + \xi\frac{\partial}{\partial z} \tag{3.1.13}$$

Substituting Eqs. (3.1.2), (3.1.9), (3.1.10), and (3.1.13) into Equation (3.1.1), we obtain the Legendre expanded multi-group form of the transport equation in 3-D Cartesian geometry [12.13] considering only fission sources:

$$\begin{aligned}
&(\mu\frac{\partial}{\partial x} + \eta\frac{\partial}{\partial y} + \xi\frac{\partial}{\partial z})\psi_g(x,y,z,\mu,\varphi) + \sigma_g(x,y,z)\psi_g(x,y,z,\mu,\varphi) = \\
&\sum_{g'=1}^{G}\sum_{l=0}^{L}(2l+1)\sigma_{s,g'\to g,l}(x,y,z)\{P_l(\mu)\phi_{g',l}(x,y,z) + 2\sum_{k=1}^{l}\frac{(l-k)!}{(l+k)!}P_l^k(\mu)\cdot \\
&[\phi^k_{\cos g',l}(x,y,z)\cos(k\varphi) + \phi^k_{\sin g',l}(x,y,z)\sin(k\varphi)]\} + \frac{\chi_g}{k_o}\sum_{g'=1}^{G}\nu\sigma_{f\,g'}(x,y,z)\phi_{g',0}(x,y,z)
\end{aligned} \tag{3.1.14}$$

Where:

μ = x direction cosine for angular ordinate
η = y direction cosine for angular ordinate
ξ = z direction cosine for angular ordinate
ψ_g = group g angular particle flux (for groups g=1,G)
ϕ = azimuthal angle constructed from $\arctan(\xi/\eta)$, with proper phase shift
σ_g = total group macroscopic cross section
l = Legendre expansion index ($l = 0, L$), L=0 or odd truncation
$\sigma_{sg'\to g,l}$ = l th Legendre moment of the macroscopic differential scattering cross section from group $g' \to g$
$P_l(\mu)$ = l th Legendre polynomial
$\phi_{g',l}$ = l th Legendre scalar flux moment for group g
$P_l^k(\mu)$ = l th, k th Associated Legendre polynomial
$\varphi^k_{\cos g',l}$ = l th, k th Cosine Associated Legendre scalar flux moment for group g
$\varphi^k_{\sin g',l}$ = l th, k th Sine Associated Legendre scalar flux moment for group g
χ_g = group fission distribution constant (neutrons)
k_o = criticality eigenvalue (neutrons)
$\nu\sigma_{f\,g}$ = group fission production (neutrons)

The flux moments, $\varphi_{g',l}$, $\varphi^k_{\cos g',l}$ and $\varphi^k_{\sin g',l}$ are defined in terms of μ' and ϕ' as:

$$\phi_{g',l}(x,y,z) = \int_{-1}^{1} \frac{d\mu'}{2} P_l(\mu') \int_0^{2\pi} \frac{d\varphi'}{2\pi} \psi_{g'}(x,y,z,\mu',\varphi') \tag{3.1.15}$$

$$\phi^k_{\cos g',l}(x,y,z) = \int_{-1}^{1} \frac{d\mu'}{2} P_l^k(\mu') \int_0^{2\pi} \frac{d\varphi'}{2\pi} \cos(k\varphi')\psi_{g'}(x,y,z,\mu',\varphi') \tag{3.1.16}$$

$$\phi^k_{\sin g',l}(x,y,z) = \int_{-1}^{1} \frac{d\mu'}{2} P_l^k(\mu') \int_0^{2\pi} \frac{d\varphi'}{2\pi} \sin(k\varphi')\psi_{g'}(x,y,z,\mu',\varphi') \tag{3.1.17}$$

Where angular flux expanded using Spherical Harmonics is

$$\begin{aligned}\psi_g(x,y,z,\mu,\varphi) &\approx \sum_{l=0}^{L}(2l+1)\{P_l(\mu)\phi_{g,l}(x,y,z) + \\ &+ 2\sum_{k=1}^{l}\frac{(l-k)!}{(l+k)!}P_l^k(\mu)[\phi^k_{\cos g,l}(x,y,z)\cos(k\varphi) + \phi^k_{\sin g,l}(x,y,z)\sin(k\varphi)]\}\cdot\end{aligned} \tag{3.1.18}$$

3.1.2 Adaptation of Subgroup Decomposition in 3D

For the Subgroup Decomposition Method (SDM) [13], we introduce the "delta" correction term that comes from a transport correction term expressed as a difference between the typical coarse group total cross section and the adaptation of angular flux as a function of energy over *h* fine group energy bins that will be projected onto a coarse group structure:

$$\delta(x,y,z,\mu,\varphi,E) = \int_{E\mathrm{h}}^{E\mathrm{h}\text{-}1} dE(\sigma_g(x,y,z) - \sigma(x,y,z,E))(\psi(x,y,z,\mu,\varphi,E)) \qquad 3.1.19)$$

Considering E_h to E_{h-1} with delta term, with deltas propagated as moments, we obtain:

$$\begin{aligned}\delta(x,y,z,\mu,\varphi,E) &= \sum_{l=0}^{L}(2l+1)\{P_l(\mu)\delta_{l,h}(x,y,z)\phi_{l,h}(x,y,z) + \\ 2\sum_{k=1}^{l}\frac{(l-k)!}{(l+k)!}P_l^k(\mu)[\delta^k_{l,h,\cos}(x,y,z)\phi^k_{\cos h,l}(x,y,z)\cos(k\varphi) &+ \delta^k_{l,h,\sin}(x,y,z)\phi^k_{\sin h,l}(x,y,z)\sin(k\varphi)]\}\cdot\end{aligned} \tag{3.1.20}$$

Where over groups E_h to E_{h-1}

$$\delta_{l,h}(x,y,z) = \frac{\int_{E_h}^{E_{h-1}} dE(\sigma_h(x,y,z) - \sigma(x,y,z,E))\phi_l(x,y,z,E)}{\int_{E_h}^{E_{h-1}} dE\phi_l(x,y,z,E)} \tag{3.1.21}$$

Which simplifies to

$$\delta_{l,h}(x,y,z) = \sigma_h(x,y,z) - \frac{\int_{E_h}^{E_{h-1}} dE\,\sigma(x,y,z,E)\phi_l(x,y,z,E)}{\int_{E_h}^{E_{h-1}} dE\,\phi_l(x,y,z,E)} \tag{3.1.22}$$

Similarly, for the cosine and sine moment terms, the formulations become:

$$\delta^k_{l,h,\cos}(x,y,z) = \sigma_h(x,y,z) - \frac{\int_{E_h}^{E_{h-1}} dE\,\sigma(x,y,z,E)\phi^k_{l,\cos}(x,y,z,E)}{\int_{E_h}^{E_{h-1}} dE\,\phi^k_{l,\cos}(x,y,z,E)} \tag{3.1.23}$$

And

$$\delta^k_{l,h,\sin}(x,y,z) = \sigma_h(x,y,z) - \frac{\int_{E_h}^{E_{h-1}} dE\,\sigma(x,y,z,E)\phi^k_{l,\sin}(x,y,z,E)}{\int_{E_h}^{E_{h-1}} dE\,\phi^k_{l,\sin}(x,y,z,E)} \tag{3.1.24}$$

Then, by convention of the SDM in terms of *C* total coarse groups (*1*,*C*) and *H* total fine groups (*1*,*H*) we have:

$$\delta_{l,c}(x,y,z) = \sigma_c(x,y,z) - \frac{\sum_{h\in c}\sigma_h(x,y,z)\phi_{l,h}(x,y,z)}{\sum_{h\in c}\phi_{l,h}(x,y,z)} \tag{3.1.25a}$$

$$\delta^k_{l,h,\cos}(x,y,z) = \sigma_c(x,y,z) - \frac{\sum_{h\in c}\sigma_h(x,y,z)\phi^k_{l,h,\cos}(x,y,z)}{\sum_{h\in c}\phi^k_{l,h,\cos}(x,y,z)} \tag{3.1.25b}$$

$$\delta^k_{l,c,\sin}(x,y,z) = \sigma_c(x,y,z) - \frac{\sum_{h\in c}\sigma_h(x,y,z)\phi^k_{l,h,\sin}(x,y,z)}{\sum_{h\in c}\phi^k_{l,h,\sin}(x,y,z)} \tag{3.1.25c}$$

So, we can define a total "delta" coarse group correction term for SDM as $\delta_c(x,y,z,\mu,\phi)$:

$$\delta_c(x,y,z,\mu,\varphi) = \sum_{l=0}^{L}(2l+1)\{P_l(\mu)\delta_{l,c}(x,y,z)\phi_{l,c}(x,y,z) + 2\sum_{k=1}^{l}\frac{(l-k)!}{(l+k)!}P_l^k(\mu)[\delta^k_{l,c,\cos}(x,y,z)\phi^k_{\cos\,c,l}(x,y,z)\cos(k\varphi) + \delta^k_{l,c,\sin}(x,y,z)\phi^k_{\sin\,c,l}(x,y,z)\sin(k\varphi)]\}\cdot \tag{3.1.26}$$

Then, the corrected transport equation is:

$$(\mu\frac{\partial}{\partial x} + \eta\frac{\partial}{\partial y} + \xi\frac{\partial}{\partial z})\psi_c(x,y,z,\mu,\varphi) + \sigma_c(x,y,z)\psi_c(x,y,z,\mu,\varphi) = \tag{3.1.27}$$

$$\sum_{c'=1}^{C}\sum_{l=0}^{L}(2l+1)\{\sigma_{s,c'\to c,l}(x,y,z)P_l(\mu)\phi_{c',l}(x,y,z)+2\sum_{k=1}^{l}\frac{(l-k)!}{(l+k)!}P_l^k(\mu)\cdot$$
$$[\sigma_{l\ s,\cos,c'\to c}^{k}(x,y,z)\phi_{\cos c',l}^{k}(x,y,z)\cos(k\varphi)+$$
$$\sigma_{l\ s,\sin,c'\to c}^{k}(x,y,z)\phi_{\sin c',l}^{k}(x,y,z)\sin(k\varphi)]\}$$
$$+\frac{\chi_c}{k_o}\sum_{c'=1}^{C}\nu\sigma_{f\ c'}(x,y,z)\phi_{c',0}(x,y,z)+\delta_c(x,y,z,\mu,\varphi)$$

Where the total coarse group cross section is

$$\sigma_{t,c'}(x,y,z)=\frac{\sum_{h'\in c'}\sigma_{t,h'}(x,y,z)\phi_{h',0}(x,y,z)}{\sum_{h\in c}\phi_{h',0}(x,y,z)} \tag{3.1.28}$$

And scattering moment cross sections are

$$\sigma_{s,c'\to c,l}(x,y,z)=\frac{\sum_{h\in c}\sum_{h'\in c'}\sigma_{s,h'\to h,l}(x,y,z)\phi_{h',l}(x,y,z)}{\sum_{h\in c}\sum_{h'\in c'}\phi_{h',l}(x,y,z)} \tag{3.1.29a}$$

$$\sigma_{l\ s,\sin,c'\to c}^{k}(x,y,z)=\frac{\sum_{h\in c}\sum_{h'\in c'}\sigma_{l\ s,\sin,h'\to h}^{k}(x,y,z)\phi_{\sin h',l}^{k}(x,y,z)}{\sum_{h\in c}\sum_{h'\in c'}\phi_{\sin h',l}^{k}(x,y,z)} \tag{3.1.29b}$$

$$\sigma_{l\ s,\cos,c'\to c}^{k}(x,y,z)=\frac{\sum_{h\in c}\sum_{h'\in c'}\sigma_{l\ s,\cos h'\to h}^{k}(x,y,z)\phi_{\cos h',l}^{k}(x,y,z)}{\sum_{h\in c}\sum_{h'\in c'}\phi_{\cos h',l}^{k}(x,y,z)} \tag{3.1.29c}$$

and fission cross sections for group c are rendered from zeroth moments:

$$\nu\sigma_{f\ c'}(x,y,z)=\frac{\sum_{h'\in c'}\nu\sigma_{f,h'}(x,y,z)\phi_{h',0}(x,y,z)}{\sum_{h\in c}\phi_{h',0}(x,y,z)} \tag{3.1.30}$$

Flux moments are as before, but with (*1*..*C*) coarse groups:

$$\phi_{C',l}(x,y,z)=\int_{-1}^{1}\frac{d\mu'}{2}P_l(\mu')\int_0^{2\pi}\frac{d\varphi'}{2\pi}\psi_{C'}(x,y,z,\mu',\varphi') \tag{3.1.31a}$$

$$\phi_{\cos C',l}^{k}(x,y,z)=\int_{-1}^{1}\frac{d\mu'}{2}P_l^k(\mu')\int_0^{2\pi}\frac{d\varphi'}{2\pi}\cos(k\varphi')\psi_{C'}(x,y,z,\mu',\varphi') \tag{3.1.31b}$$

$$\phi_{\sin C',l}^{k}(x,y,z)=\int_{-1}^{1}\frac{d\mu'}{2}P_l^k(\mu')\int_0^{2\pi}\frac{d\varphi'}{2\pi}\sin(k\varphi')\psi_{C'}(x,y,z,\mu',\varphi') \tag{3.1.31c}$$

The broad group cross section data is generated from the fine group cross section data and a fine group flux spectrum using Equations (3.1.28) to (3.1.30). The initial process can be started by using a flat fine

group flux spectrum. Broad group fluxes and flux moments are then obtained by solving the collision-term-corrected transport equation (Equations (3.1.27) and (3.1.31)) with the standard transport sweep algorithm. Thereafter, the fine group fluxes are updated by solving the one-pass fine group transport equation (Equation (3.1.32)).

$$\begin{aligned}\widehat{\mathbf{\Omega}} \cdot \nabla\psi_h(\vec{r},\Omega) + \sigma_h(\vec{r})\psi_h(\vec{r},\Omega) \\ &= \frac{1}{4\pi k}\sum_{c'=1}^{C} R_{f,c'\to h}(r)\phi_{c'}(\vec{r}) \\ &+ \sum_{c'=1}^{C}\sum_{l=0}^{L}(2l+1)\{P_l(\mu)\phi_{l,c'}(\vec{r})R_{s,l,c'\to h} \\ &+ 2\sum_{k=1}^{l}\frac{(l-k)!}{(l+k)!}P_l^k(\mu)\big[\phi_{cos,l,c'}(\vec{r})\cos(k\varphi)\,R^k_{s\,cos,l,c'\to h} \\ &+ \phi_{sin,l,c'}(\vec{r})\sin(k\varphi)\,R^k_{s\,sin,l,c'\to h}\big]\}\end{aligned} \tag{3.1.32}$$

Where the R's are defined by Equations (3.1.33), and (3.1.34).

$$R_{f,c'\to h} = \chi_h \frac{\sum_{h'\in C'} \nu\sigma_{f,h'}\phi_{h'}}{\sum_{h'\in C'}\phi_{h'}} \tag{3.1.33}$$

$$R^m_{s,l,c'\to h} = \frac{\sum_{h'\in C'}\sigma_{slh'\to h}\phi^m_{l,h'}}{\sum_{h'\in C'}\phi^m_{l,h'}} \tag{3.1.34a}$$

$$R^m_{s\,cos,l,c'\to h} = \frac{\sum_{h'\in C'}\sigma_{slh'\to h}\phi^m_{cos,l,h'}}{\sum_{h'\in C'}\phi^m_{cos,l,h'}} \tag{3.1.34b}$$

$$R^m_{s\,sin,l,c'\to h} = \frac{\sum_{h'\in C'}\sigma_{slh'\to h}\phi^m_{sin,l,h'}}{\sum_{h'\in C'}\phi^m_{sin,l,h'}} \tag{3.1.34c}$$

Details on the *R* coefficients and the subgroup decomposition method can be found in reference [13]. Note Equation (3.1.32) only requires a single iteration, because the fission source and the scattering source terms are calculated using the previous obtained broad group fluxes and flux moments and the *R* coefficients, instead of the fine group fluxes and flux moments. Both source terms are fixed. One transport sweep is sufficient to acquire the fine group angular fluxes, since no iteration processes are required on the convergence of the fission source or scattering source. Once the one-pass sweep is completed, then the fine group flux moments are used to calculate the newest broad group cross sections, again as noted in Equations (3.1.28) to (3.1.30). Then, these updated broad group cross sections are used in the next inner and outer transport sweeps to result in another set of coarse group fluxes and a new estimated k-effective. Pseudo code for the entire iteration process is summarized in Figure in the section 3.3.

Task 3.2 Generate 3D benchmark problems

The present benchmark consists of whole-core heterogeneous problems in 2D and 3D hexagonal geometries. A radial cross section of the core is shown in Fig. 3.2.1a. The reactor core is modeled as a

regular hexagon with a flat-to-flat distance of 436.4768[2] cm and is completely filled by a hexagonal lattice consisting of prismatic fuel blocks, control blocks, and reflector blocks. These hexagonal blocks are all of uniform size with a flat-to-flat distance of 36 cm, except at the periphery in which case there are half blocks along the core edges and 1/3 blocks at the corners.

The lattice block configuration for the core is shown in Fig. 3.2.1b. Regions 1 through 4 in this figure are fuel blocks of increasing enrichment; regions 5 and 6 are control blocks; regions 7 and 8 are replaceable and permanent reflector blocks, respectively. Vacuum boundary conditions are assigned on the external boundaries of the core.

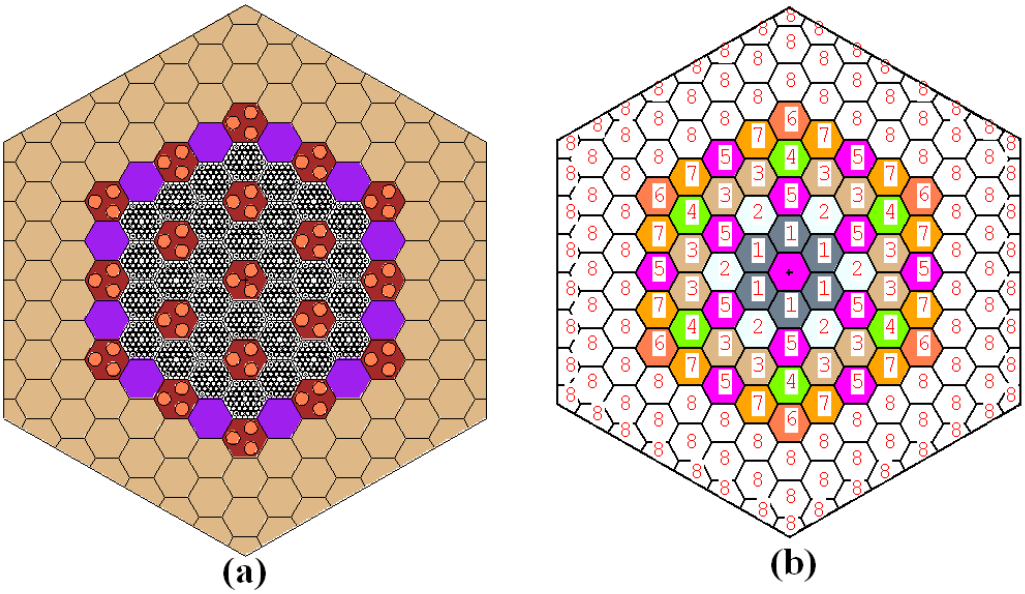

Fig. 3.2.1. The whole core structure and configuration of the simplified HTTR benchmark. (a) Whole core layout, (b) Region indexing in the whole core.

The four fundamental block geometries are shown in Fig. 3.2.2: fuel blocks, control blocks, solid reflector blocks, and reflector blocks with coolant holes. Each fuel block contains 33 identical fuel pins and 3 BP rods. The fuel enrichment within any single block is uniform but varies from block to block in the core. Each control block contains three removable control rods, whose centers are 10.8 cm from the block center. The reflector blocks with coolant holes are only used in the top and bottom reflector layers of the 3D model. All geometric dimensions are listed in Table 3.2.1.

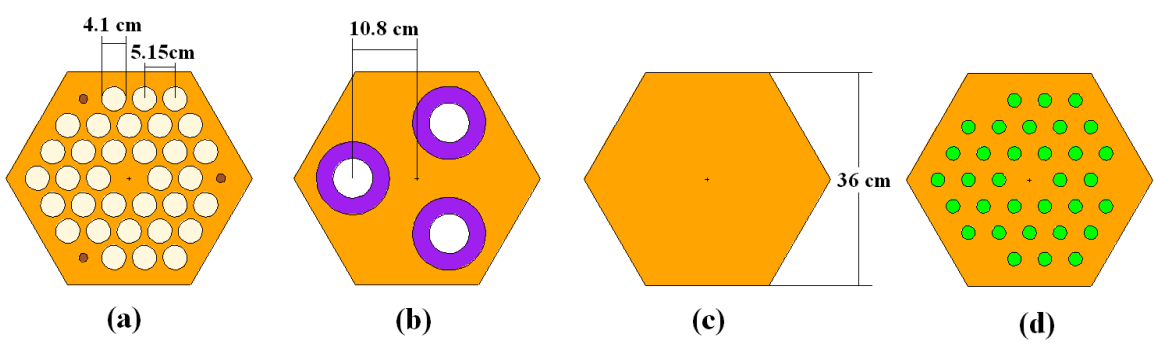

[2] truncated from $7 \times 36\sqrt{3}$

Fig. 3.2.2. Block structures: (a) fuel blocks, (b) control blocks, (c) reflector blocks, (d) reflector blocks with coolant holes.

There are a total of 13 materials used in the benchmark problem: seven fuel materials with varying enrichment (listed in Table 3.2.2); four graphite materials corresponding to the graphite in fuel blocks, control blocks, permanent reflector blocks, and replaceable reflector blocks; and two absorber materials for the BP rods and control rods.

Table 3.2.1. Simplified HTTR benchmark geometry parameters

Number of fuel columns	30
Number of control rod columns	19
Number of replaceable reflector columns	12
Number of permanent reflector columns (whole/half/third blocks)	108 (66/36/6)
Number of layers (3D)	9
Number of layers for active core (3D)	5
Flat-to-flat core width	436.4768 cm
Flat-to-flat block width	36 cm
Block height (3D)	58 cm
Number of Fuel Pins per fuel block	33
Number of BP rods per fuel block	3
Fuel pin (BP rod) pitch	5.15 cm
Fuel pin diameter	4.1 cm
BP rod diameter	1.5 cm
Coolant hole diameter (in top and bottom reflector block)	2.3 cm
Control rod diameter	12.3 cm
Control rod inner diameter	6.7 cm
Distance from control rod center to block center	10.8 cm

Table 3.2.2. Enrichments for different fuel types

Fuel type	1	2	3	4
Enrichment (%)	3.4	4.8	5.2	6.3
Fuel type	5	6	7	
Enrichment (%)	6.7	7.9	9.9	

The fundamental blocks described above are the same for both the two-dimensional and three-dimensional problems. The radial cross section for active cores of both the 2D and 3D models are the same, as shown in Fig. 3.2.1. The 2D problem consists of a single layer with specular reflection boundary conditions on the top and bottom, whereas the 3D problem consists of nine layers: two top reflector layers, five fuel layers constituting the active core height, and two bottom reflector layers as shown in Fig. 3.2.3. The radial reflector columns are uniform axially. In the 3D model, the fuel type distribution in the active core as a function of the axial layer and radial region is found in Table 3.2.3. See Fig. 3.2.1b for the radial region indexing and Fig. 3.2.2 for the axial layer map. For the top and bottom reflector layers, the layout is the same as the radial cross section of the active core in Fig. 3.2.1a, except the reflector blocks with coolant (Fig. 3.2.2d) are positioned in regions 1-4 instead of fuel blocks. The fuel type distribution in the 2D model is also shown in Table 3.2.3.

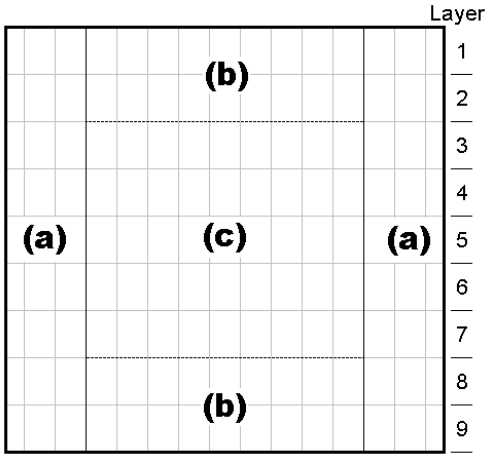

Fig.3.2.3. Axial cross section of the 3D core.
(a) Radial reflector, (b) top and bottom reflectors, (c) active core.

Table 3.2.3. Radial and axial distribution of fuel blocks – fuel type in each fuel region and layer (see Fig. 1b)

		Fuel region 1	**Fuel region 2**	**Fuel region 3**	**Fuel region 4**
2D		2	3	4	5
	Layer 3	5	6	7	7
	Layer 4	3	4	5	6
3D	**Layer 5**	2	3	3	4
	Layer 6	1	1	2	2
	Layer 7	1	1	2	2

A two and three dimensional numerical benchmark problems typical of high temperature gas cooled prismatic cores have been developed [10]. Additionally, we have included single cell and single block benchmark problems. These problems were derived from the HTTR startup experiment by simplifying the geometry and material specification of the original experiment while retaining the heterogeneity and major physics properties of the core from a neutronics viewpoint. Control rod configurations considered in the reference were all-rods-in, partially-controlled and all-rods-out.

A six-group material (macroscopic) cross section library was developed for the benchmark problems using the lattice depletion transport code HELIOS. Using this library, Monte Carlo solutions were provided for all configurations considered. These solutions included the core eigenvalue, block-averaged fission density, local peaking factors, absorption density in burnable poison and control rods, and fuel pin fission density distribution in selected blocks. Reference solutions were also provided for single fuel pin cell and single fuel block configurations.

Task 3.3 Implement the theory into the selected codes in 3D and solve 3D benchmarks

3.3.1 SDM Iteration Scheme

The SDM iterative process to solve a k-effective problem is described in
Figure . Table shows the notations that are used in the figure.

Table 3.3.1: Notations used in SDM implementation discussion.

Variable	Definition
h	fine-group index, h=1,H
C	broad-group index, c=1,C
Xs	cross section
BG	broad-group
FG	fine-group
R	subgroup cross sections
LBE	Linear Boltzmann Equation
RE	calculated relative error (see below)

The convergence of the solution is based on the iterative relative errors of various parameters, as indicated in
Figure . Equations (3.3.1) below show how these errors are calculated.

$$\mathrm{RE}(k_{eff}) = \frac{\left|k_{eff}^{(i-1)} - k_{eff}^{(i)}\right|}{k_{eff}^{(i)}} \tag{3.3.1a}$$

$$\mathrm{RE}(\phi_h) = \frac{\left|\phi_h^{(i-1)}(r) - \phi_h^{(i)}(r)\right|}{\phi_h^{(i)}(r)} \tag{3.3.1b}$$

$$\mathrm{RE}(\sigma_{t,h}) = \frac{\left|\sigma_{t,h}^{(i-1)}(r) - \sigma_{t,h}^{(i)}(r)\right|}{\sigma_{t,h}^{(i)}(r)} \tag{3.3.1c}$$

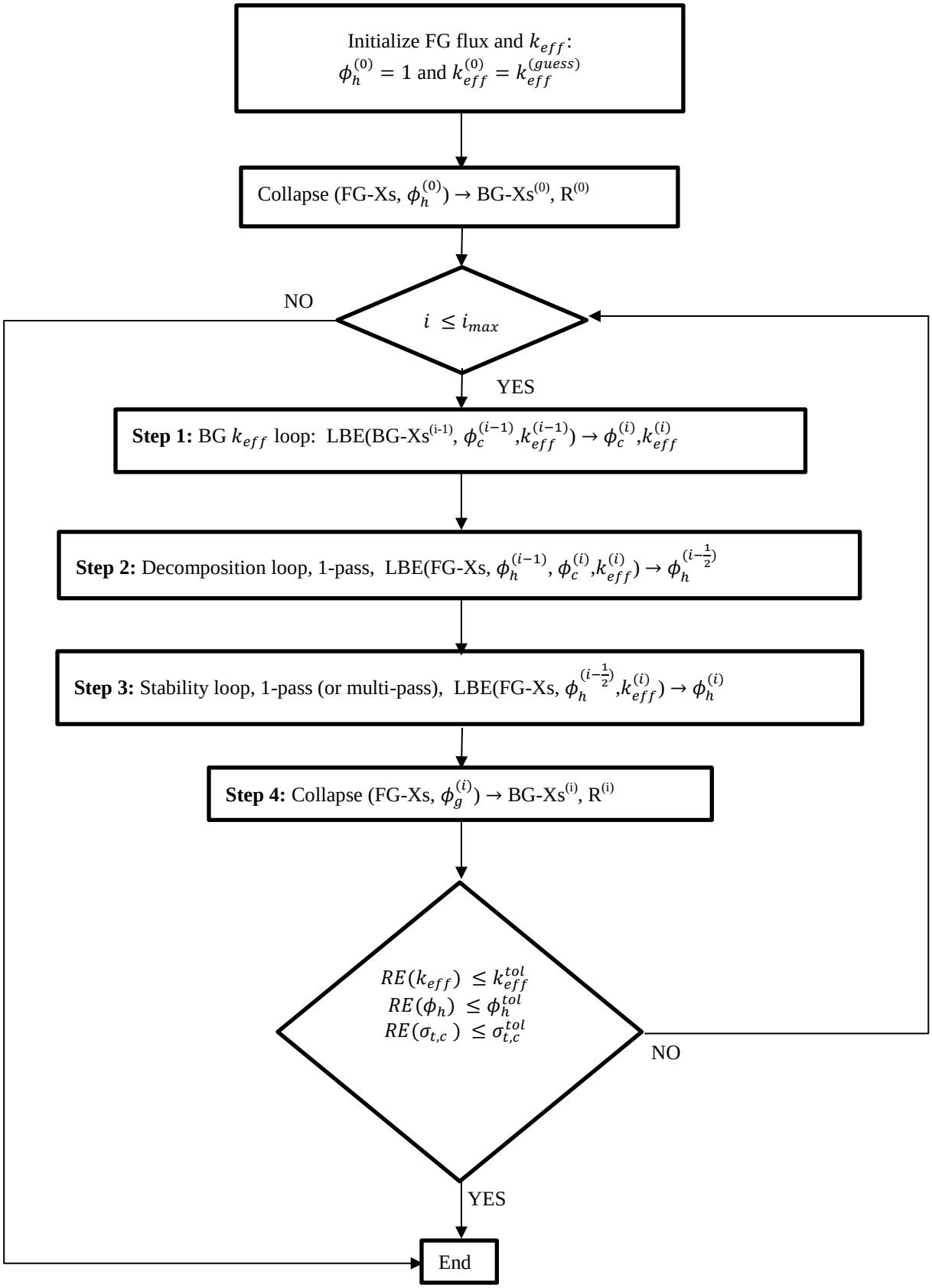

Figure 3.3.1: TITAN SDM implementation flow chart. (Figure key located in Table)

Step 3, the "stability loop" has not yet been discussed as it was added later in the implementation of the SDM into the TITAN code. The stability loop is also a fixed source problem, much like the decomposition loop; therefore it only requires 1-pass. There is an option in the user input file that allows this step to be multi-pass if the user chooses so. Equation (3.3.2) shows the transport equation for the stability loop.

$$\begin{aligned}\widehat{\mathbf{\Omega}} \cdot \nabla\psi_h^{(i)}(\vec{r},\Omega) + \sigma_h(\vec{r})\psi_h^{(i)}(\vec{r},\Omega) \\ = \frac{\chi_h}{4\pi k}\sum_{c'=1}^{C} \nu\sigma_{f,c'}(\vec{r})\phi_{c'}(\vec{r}) \\ + \sum_{h'=1}^{H}\sum_{l=0}^{L}(2l+1)\sigma_{s,l,h'\to h}(\vec{r})\{P_l(\mu)\phi_{l,h'}^{\left(i-\frac{1}{2}\right)}(\vec{r}) \\ + 2\sum_{k=1}^{l}\frac{(l-k)!}{(l+k)!}P_l^k(\mu)\left[\phi_{cos,l,h'}^{\left(i-\frac{1}{2}\right)}(\vec{r})\cos(k\varphi) + \phi_{sin,l,h'}^{\left(i-\frac{1}{2}\right)}(\vec{r})\sin(k\varphi)\right]\}\end{aligned} \tag{3.3.2}$$

The material-based fine group library (*FGXs*) is a user input, and doesn't change in the iteration process. The broad group cross section data and *R* factors (*BG-Xs, R*) are location-dependent, and they are re-collapsed from the fine group library at the beginning of each iteration using the updated fine group fluxes as weighting factors. Since the fine group fluxes are location dependent, broad-group cross sections and subgroup cross sections are also location dependent, which means each fine mesh has its individual cross-section table and associated *R* coefficients. The memory requirements to store fine-mesh broad-group data could be very high for large problems. A potential option for memory savings involves using coarse-mesh averaged cross sections and *R* values, instead of fine-mesh cross-section data. For example, a coarse mesh with three materials: water, fuel, and clad could require three material-based coarse-group cross-section tables, which are collapsed using three material-averaged fine-group flux spectra in the coarse-mesh, or simply, just one averaged coarse-mesh fine-group flux spectrum.

3.3.2 Memory Requirement Estimation.

Here we provide an estimation of additional memory requirement for implementing SDM. Table shows the variables used in the estimation.

Table 3.3.2: List of variables used for memory requirement estimation.

Variable	Definition
N	number of fine meshes
H	total number of fine groups
C	total number of broad groups
L	scattering Pn order

The total additional memory requirement can be estimated by Equation (3.3.3), note that all values are real numbers.

$$Memory = N \times C \times C \times (L+1) + H \times C \times (3L+4) + N \times C \times 3 \tag{3.3.3}$$

The main memory requirement is the first term of Equation (3.3.3), which is used to store the fine-mesh based broad group scattering cross section tables. The second term is used to store *R* terms. The *R* terms are also fine-mesh dependent. However, since they are only calculated once in the 1-pass fine group LBE, we can calculate them on-the-fly for each fine mesh. This eliminates the need to store R's for every fine

mesh. The last term is the storage requirement for total and fission cross sections, and nu-bar data (average fission neutrons per fission).
We assume the fine group library is the 47-group BUGLE library with P3 scattering order. The fine library is collapsed into an 8-group library. For a problem model with 50x50x50=125,000 fine meshes, the required additional memory is 133.3 MB for 4-byte real numbers.

V. CONCLUSIONS

The efficient solution of the transport equation (or its diffusion approximation) requires condensation of cross sections into a coarse energy group structure. The accuracy of the condensed cross sections is strongly affected by the assumptions made during the condensation process. Particularly important is the assumption that the energy and angular dependence of the flux are separable when generating the condensed total cross section. Strongly absorbing media, local material interfaces, and external core boundaries introduce high levels of flux anisotropy and steep flux gradients which invalidate this assumption.

The consistent generalized energy condensation theory explicitly accounts for the angular dependence of the condensed total collision cross section. This is accomplished by separating the collision cross section into a group average and a variation term, and treating the variation term as a coupling correction to the source. By expanding the coupling correction in energy and angle, the condensed solution becomes exactly consistent with the uncondensed solution. The use of the generalized energy condensation theory also allows correcting for the core environment effect which is an inevitable source of error for all condensation methods. This done by unfolding the condensed flux into an uncondensed group structure with accuracy restricted only by the order of energy expansion. Because the higher-order energy moments are obtained with minimal additional solution time, this allows the unfolded flux to be obtained very efficiently. As a result, the new method provides solutions which exhibit the accuracy of the uncondensed solution (i.e., fine-group) with a solution time characteristic of the condensed solution (coarse-group), reduces the number of groups necessary for the core calculation, and results in significant computational savings.

The subgroup decomposition method solves for the fine-group flux spectrum in a coarse-group calculation in a more direct manner than the consistent generalized energy condensation theory. The method does not require the generation of energy expansion moments for the cross sections or solving higher-moment equations for the angular flux. Rather, the method directly couples the consistent coarse-group criticality calculation to a set of fixed-source decomposition sweeps which requires less memory and computation time than energy-expansion based methods.

The SGD algorithm is very sensitive to specified convergence criteria and tolerance levels. It was necessary to implement coarse-mesh-wise regional tolerance into the TITAN code to handle problems with sharp flux gradients; specifically with regions that could potentially produce zero (or very low) fluxes. This is primarily due to the fact that TITAN uses only single precision values when doing error calculations. This issue was not observed in the 1D transport code by Douglass and Rahnema [13] because their code operated in double precision.

For a solution to be converged, it was not necessary to converge on both the subgroup eigenvalue and coarse-group cross section. It was sufficient to only converge on the subgroup eigenvalue, assuming that the coarse-group fluxes and eigenvalue calculations had converged within the coarse-group transport sweeps.

The SGD algorithm works very effectively and accurately for both the 1D and 2D problems presented here. The 1D problem showed substantially greater speedups, though both problems yielded accurate results.

It was noticed that coarse-group structure had an effect on calculation time; for too few or too many groups, the computation required more time to converge. Too few groups cause issues with preserving the energy-angle coupling, due to the large amount of information that must be preserved with only a few number of groups. Too many groups slow down computation because more transport sweeps must be done. It was observed that when the epithermal region was too refined it caused a lower accuracy in the eigenvalue.

It is shown that the transport based subgroup decomposition method is a non-synthetic acceleration technique for solving fine-group eigenvalue transport equations. It is capable of achieving direct fine-group transport solution (within the convergence limit) provided that the convergence criteria for the coarse group calculations are tighter (e.g., by one order of magnitude). A new hybrid subgroup decomposition method is also developed to further accelerate the convergence. This method in essence is an extension of the subgroup decomposition method which directly couples a consistent new coarse-group quasi transport criticality calculation with a set of fixed-source transport decomposition sweeps to obtain the fine-group solution more efficiently.

Finally, it is demonstrated that the SGD algorithm can easily be incorporated into any 3-D Sn transport code. It is concluded that, depending on the problem, significant speedup is attainable. Future studies are needed for utilization of the SGD for real-life reactor problems.

REFERENCES

1. Rahnema, F., Douglass, S., and Forget, B., "A Generalized Energy Condensation Theory," *Nucl. Sci. Eng*, **160,** No. 1, 41-58 (2008).
2. Lewis, E., Miller, W., Computational Methods of Neutron Transport, American Nuclear Society, La Grange Park, Illinois (1993).
3. Mosher, S., and Rahnema, F., "The Incident Flux Response Expansion Method for Heterogeneous Coarse Mesh Transport Problems," *Transport Theory and Statistical Physics* **35**. 55-86 (2006).
4. Douglass, S., and Rahnema, F., "Cross Section Recondensation Method via Generalized Energy Condensation Theory," Technical Note, *Ann. Nucl. Energy*, **38**, 2105–2110 (2011)
5. Pounders, J., Rahnema, F., and Stamm'ler, R. J. J., "Stochastically Generated Multigroup Cross Sections," PHYTRA1: First International Conference on the Physics and Technology of Reactors and Applications, Marrakech, Morocco (2007).
6. Sterberntz, J. W., Phillips, B., Sant, R. L, Chang, G. S., and Bayless P.D , "Reactor Physics Parametric and Depletion Studies in Support of TRISO Particle Fuel Specification for the Next Generation Nuclear Plant", Idaho National Engineering and Environmental Laboratory, INEEL/EXT-04-02331 (2004).
7. Lee, C.H., Zhong, Z., Taiwo, T.A., Yang, W. S., Smith, M.A., and Palmiotti G., "Status of Reactor Physics Activities on Cross Section Generation and Functionalization for the Prismatic Very High Temperature Reactor, and Development of Spatially-Heterogeneous Codes", ANL-GenIV-075 (2006).

8. Douglass, S., and Rahnema, F., "Consistent Generalized Energy Condensation Theory," *Ann. Nucl. Energy*, **40**, 200–214 (2012).
9. Simeonov, T., Release Notes – Helios System Version 1.8, Studsvik Scandpower Report, SSP-03/221 (2003).
10. Zhang, Z., Rahnema, F., et al., Simplified Two and Three Dimensional HTTR Benchmark Problems, Ann. Nucl. Energy 38, 1172-1185 (2011).
11. Sjoden G and Haghighat A, PENTRAN-A 3-D cartesian parallel SN code with angular, energy, and spatial decomposition, Proceedings of the Joint International Conference on Mathematical Methods and Supercomputing in Nuclear Applications. Vol. 2, pp. 1267-1276 (1997).
12. Yi, C., Haghighat, A., PENMSH-XP: A 3-D Mesh Generator for PENTRAN, Version 1.5b, University of Florida (2008).
13. Douglass, S., and Rahnema, F., "Subgroup Decomposition Method," *Ann. Nucl. Energy*, **48**, 84-101 (2012).
14. Yi, C., TITAN: A 3-D Deterministic Radiation Transport Code User Manual Version 1.29, Version 1.29, Rev. 1, University of Florida (2012).
15. Bell, G., Glasstone, S., Nuclear Reactor Theory, Malabar, Florida: Krieger (1985).

Status Summary of Tasks

Milestone/Task Description	Percent complete
1.1 Derive new equations in general geometry with energy-angle coupling	100%
1.2 Generate 1D benchmark problems for optically thin reactors	100%
1.3 Develop 1D transport implementation	100%
1.4 Generate collapsed cross sections from continuous energy	100%
1.5 Use selected codes to generate standard multi-group solutions	100%
2.1 Implement the theory into the selected codes in 1D and solve 1D benchmarks	100%
2.2 Extend the numerical formulation into 2D	100%
2.3 Generate 2D benchmark problems for optically thin reactors	100%
2.4 Implement the theory into the selected codes in 2D and solve 2D benchmarks	100%
2.5 Explore a 1D diffusion approximation for the new multi-group theory	100%
2.6 Expert Review of the status of the project	100%
3.1 Extend the Numerical Formulation to 3D	100%
3.2 Generate 3D benchmark problems for optically thin reactors	100%
3.3 Implement the theory into the selected codes in 3D and solve 3D benchmarks	100%